Highlights

- a new model has been developed to describe the hardening recovery during annealing
- a temperature dependent recovery variable counteracts the effect of the hardening
- the model has been applied to the thermomechanical response of 316L steel
- the proposed modeling approach is intended to simulate the welding process

Thermally-activated hardening recovery of thermo-elasto-plastic metals during annealing: constitutive modeling for the simulation of welding process

L. Mouelle, F. Praud, G. Chatzigeorgiou, F. Meraghni, J. Serri, E. Fleury*

Université de Lorraine, CNRS, Arts et Métiers ParisTech, LEM3, F-57000, Metz, France

Abstract

In this paper, a new thermodynamically-consistent modeling approach, dedicated to welding applications, is presented to describe the phenomenon of hardening recovery in metals during annealing. The constitutive equations are based on a classical thermo-elasto-plastic formulation, which is enhanced by a new recovery variable counterbalancing the effect of the hardening through a temperature-dependent evolution law. The identification of the model parameters is achieved through experimental compressive tests and heat treatments on 316L austenitic stainless steel. Finally, numerical simulations considering various thermomechanical loading configurations are carried out to evaluate the capabilities and limits of the model, which are furthermore illustrated in the context of welding applications through a FE example.

Keywords: Constitutive model, Plasticity, Hardening recovery, Annealing, Welding, Thermomechanical behavior

*Corresponding author
Email address: eric.fleury@univ-lorraine.fr (E. Fleury)

1. Introduction

Integrating the thermomechanical behavior of metallic materials into Finite Element (FE) simulations of multipass welding process plays a major role for the understanding and the prediction of internal residual stresses and plastic distortions in welded engineering structures (Lindgren et al., 1999; Depradeux, 2004; Goldak and Akhlaghi, 2005; Lindgren, 2007; Leggatt, 2008). Previous studies demonstrated that the choice of the hardening law in thermo-elasto-plastic models has an important influence on the accuracy of the predicted results (Mullins and Gunnars, 2009; Muránsky et al., 2012a; Joosten and Gallegillo, 2012). In addition, the local plastic strain associated with high local temperature in multipass welding may lead to a softening behavior, where the yield strength can potentially be restored to its original value (Petkovic et al., 1979; Keavey et al., 2010; Yu et al., 2015; Chetra Mang and Hindili, 2017).

From a metallurgical point of view, this loss of hardening is caused by the recovery mechanism, for which a plastically deformed metal can restore its initial properties. Indeed, thermally activated processes such as solid-state diffusion, as well as rearrangement and annihilation of dislocations occur when metals are heated up to a certain temperature (Suwas and Ray, 2014). During the recovery stage, the annihilation of dislocations previously introduced by the plastic deformation leads to a reduction of the internal energy and tends to favor strain-free grains. If plastic deformation and recovery occur independently, this is referred to as *static recovery*. On the contrary, if both mechanisms occur simultaneously, as it is the case during welding,

this is referred to as *dynamic recovery* (Humphreys, 2017). Moreover, the recrystallization stage may be triggered either simultaneously or after the recovery stage (Stüwe et al., 2002), followed by the grain growth stage. The recrystallization and grain growth mechanisms are considered negligible in the modeling approach employed in this study and will be discussed in section 5. It is important to note that the term of annealing is a synecdoche that appears in different studies to describe the recovery mechanism, whereas it is normally defined as a global term for metallurgical heat treatment describing the recovery, recrystallization and grain growth.

Given the previous mentioned points, it is crucial to consider the phenomenon of recovery, or so-called *annealing*, to describe the softening behavior of a welded material through its loss of hardening memory. Different authors studied by means of FE calculations the influence of recovery on AISI 316LN austenitic stainless steel for prediction of residual stresses through phenomenological models using rate-independent plasticity with mixed isotropic-kinematic hardening law (Smith et al., 2009; Muránsky et al., 2012b; Smith et al., 2012; Muránsky et al., 2015). In these studies, two temperature thresholds T_1 and T_2 ($T_1 < T_2$) have been set. Above a lower temperature T_1, the material ceases to exhibit any further isotropic hardening but does not lose it. Above T_2, the equivalent plastic strain, is instantaneously set to zero, removing any prior isotropic hardening. Depradeux and Coquard (2018) used the same concept of the so-called *two-stage annealing*, considering that the equivalent plastic strain is multiplied by a factor equal to $\frac{T_2-T}{T_2-T_1}$ when $T_1 < T < T_2$. Despite their efficiency, these approaches display a lack of physical signifi-

cance, since the recovery is a continuous time-dependent mechanism. The two-stage annealing concept considers only the spatially reached temperature and does not account for the time during which the temperature is held constant (instantaneous recovery).

To overcome this limitation, rate-dependent plasticity models (viscoplasticity) established within the framework of thermodynamics, and including a viscous function or potential with rate-dependent dynamic and/or static recovery terms (viscous recovery) were integrated (Chaboche and Nouailhas, 1989; Razakanaivo and Waeckel, 1999; Chaboche, 2008; Besson et al., 2010). Although such approaches provide predictive results, they involve a large set of temperature-dependent parameters, that requires identification through laborious experimental tests such as stress relaxation or creep.

Furthermore, dislocation-based models such as the Kocks-Mecking-Estrin (KME) model are used to predict the mechanical behavior of metallic materials for a wide range of temperatures (Mecking and Kocks, 1981; Estrin and Mecking, 1984; Kocks and Mecking, 2003; Blaizot et al., 2016; Lin et al., 2018; Yuan et al., 2019). Voyiadjis and Abed (2005) developed a model accounting for the effect of the dislocation density evolution on the thermomechanical response of metals with different crystal structures at low and high strain rates and temperatures. Voyiadjis et al. (2019) recently modified this model by adding a specific term for modeling dynamic strain aging, which may also have a significant influence on the thermomechanical behaviors of metals. In addition to the physical concepts of dislocation interactions mechanism

and thermal activation energy, a mathematical expression of the Weibull distribution related to a physically-based mechanism of dislocation density evolution is used to derive the constitutive equations of the model. Despite bringing a physical basis, all these models require to know the initial dislocation density from TEM (*Transmission Electron Microscopy*) measurements, and microstructural parameters whose values are not necessarily referenced for all materials. To a lesser extent, it also necessitates to realize uniaxial loading tests at different temperatures and strain rates, as well as to adjust a large set of parameters (Nes, 1997; Lindgren et al., 2008, 2017).

In this work, a new constitutive modeling approach lying into the framework of thermodynamics is proposed to account for a rate-dependent hardening recovery in a classical thermo-elasto-plastic formulation under the small strains assumption. In this purpose, a new recovery variable (internal state variable), associated with an isotropic hardening function, is introduced into the constitutive equations. This recovery variable gradually cancels the effect of the hardening variable according to a temperature-dependent evolution law. The latter involves a reduced number of parameters that can be conveniently identified from uniaxial thermomechanical tests.

This paper is structured as follows: the second section introduces the constitutive equations and the thermodynamical framework of the proposed model. The third section focuses on the experimental procedure and the identification strategy of the model parameters. The fourth section presents examples of numerical simulations, where the material is subjected to var-

ious thermomechanical loading paths. A three-dimensional FE example is also presented to illustrate the model capabilities in the context of welding applications. The fifth section discusses the possible perspectives related to this work, before concluding in the last section.

In this work, the following notation is adopted: bold and blackboard symbols denote second and fourth order tensors, respectively, whereas other symbols are scalar quantities. The twice contracted and dyadic products are given by:

$$\boldsymbol{A} : \boldsymbol{B} = A_{ij}B_{ij}, \quad (\mathbb{A} : \boldsymbol{B})_{ij} = A_{ijkl}B_{kl}, \quad (\boldsymbol{A} \otimes \boldsymbol{B})_{ijkl} = A_{ij}B_{kl}.$$

Moreover, all the second order tensors are symmetric ($A_{ij} = A_{ji}$) and all the fourth order tensors have at least the minor symmetries ($A_{ijkl} = A_{jikl} = A_{ijlk}$). Consequently, they can be respectively reduced to 6×1 and 6×6 matrices according to the Voigt notation. $\boldsymbol{I}$ represents the second order identity tensor. The operators $\mathrm{hyd}(\boldsymbol{\sigma})$ and $\mathbf{Dev}(\boldsymbol{\sigma})$ designate the hydrostatic pressure and the deviatoric part of a stress tensor $\boldsymbol{\sigma}$, respectively, while $\mathrm{eq}(\boldsymbol{\sigma})$ is the equivalent Von Mises stress:

$$\mathrm{hyd}(\boldsymbol{\sigma}) = \frac{1}{3}\mathrm{tr}(\boldsymbol{\sigma}),$$

$$\mathbf{Dev}(\boldsymbol{\sigma}) = \boldsymbol{\sigma} - \mathrm{hyd}(\boldsymbol{\sigma})\boldsymbol{I},$$

$$\mathrm{eq}(\boldsymbol{\sigma}) = \sqrt{\frac{3}{2}\Big(\mathbf{Dev}(\boldsymbol{\sigma}) : \mathbf{Dev}(\boldsymbol{\sigma})\Big)}.$$

2. Constitutive equations and thermodynamical framework

2.1. State laws

The present model is based on classical thermo-elasto-plastic constitutive equations (Lemaître and Chaboche, 1990) including a temperature-independent isotropic hardening and the thermal expansion. The observable state variables of the proposed model are the total strain $\boldsymbol{\varepsilon}$ and the absolute temperature T, while the plasticity-related internal state variables are the plastic strain $\boldsymbol{\varepsilon_p}$ and the hardening variable p, which is also referred to as the equivalent plastic strain. To represent the hardening recovery mechanism, an additional internal state variable β, later referred as the *recovery variable* or *softening variable*, is utilized. The latter is introduced in the Helmholtz free energy potential as follows:

$$\rho\psi(\boldsymbol{\varepsilon}, T, \boldsymbol{\varepsilon_p}, p, \beta) = \frac{1}{2}\big(\boldsymbol{\varepsilon} - \boldsymbol{\varepsilon_p} - \boldsymbol{\varepsilon_{th}}(T)\big) : \mathbb{C} : \big(\boldsymbol{\varepsilon} - \boldsymbol{\varepsilon_p} - \boldsymbol{\varepsilon_{th}}(T)\big) + \int_0^{p-\beta} R(\xi)\ \mathrm{d}\xi \ + \ \rho\psi_0(T). \quad (1)$$

In the above equation, ρ is the mass density, considered as constant under the small strains assumption. $\mathbb{C}$ is the fourth order stiffness tensor classically formulated for bulk isotropic materials and is thus defined by the Young modulus E and the Poisson ratio ν. $\boldsymbol{\varepsilon_{th}}$ stands for the thermal strain, usually expressed for an isotropic material as:

$$\boldsymbol{\varepsilon_{th}}(T) = \alpha \boldsymbol{I}(T - T_0), \quad (2)$$

where α and T_0 denote the coefficient of thermal expansion and the reference temperature, respectively. In equation (1), R represents the hardening function, defined in the present model by an exponential-linear law (Lemaître

and Chaboche, 1990):

$$R(\xi) = Q_1\big(1 - \exp(-b\xi)\big) + Q_2\xi, \tag{3}$$

where Q_1, Q_2 and b are material parameters, while ξ is the argument of the function. Note that any other form can be used for $R(\xi)$, as long as this function is monotonically increasing and defined null at $\xi = 0$. The last term in equation (1), $\rho\psi_0(T)$, depicts the calorific energy, which is a temperature-dependent function given in Appendix A.

Following the classical thermodynamical derivation procedure, it yields the usual expression for the stress:

$$\boldsymbol{\sigma} = \rho\frac{\partial\psi}{\partial\boldsymbol{\varepsilon}} = \mathbb{C} : \big(\boldsymbol{\varepsilon} - \boldsymbol{\varepsilon_p} - \boldsymbol{\varepsilon_{th}}(T)\big), \qquad -\boldsymbol{\sigma} = \rho\frac{\partial\psi}{\partial\boldsymbol{\varepsilon_p}}, \tag{4}$$

and the thermodynamic forces:

$$\rho\frac{\partial\psi}{\partial p} = R(p-\beta), \qquad \rho\frac{\partial\psi}{\partial\beta} = -R(p-\beta). \tag{5}$$

From equation (5), it can be observed that, unlike classical plasticity models, the hardening function now depends on the difference between the hardening and the recovery variables, p and β, respectively. From a phenomenological point a view, the hardening variable p represents the effect of the generated dislocations (Aifantis, 1987; Voyiadjis and Abed, 2005), while the recovery variable β represents the effect of the dislocations that will rearrange and annihilate each others. Thus, β plays the role of an antagonist variable with respect to the internal variable p. Additionally, the entropy is defined by:

$$s = -\frac{\partial\psi}{\partial T}, \tag{6}$$

whose analytical expression is given in Appendix A.

2.2. Evolution laws

The second law of thermodynamics implies that the mechanical dissipation has to be always positive or null through the Clausius-Duhem inequality given by:

$$\begin{aligned}\dot{\Phi} &= \dot{W}_\varepsilon - \rho(\dot{\psi} + s\dot{T}) \geq 0 \\ &= \boldsymbol{\sigma} : \dot{\boldsymbol{\varepsilon}} - \rho\left(\frac{\partial \psi}{\partial \boldsymbol{\varepsilon}} : \dot{\boldsymbol{\varepsilon}} + \frac{\partial \psi}{\partial T}\dot{T} + \frac{\partial \psi}{\partial \boldsymbol{\varepsilon_p}} : \dot{\boldsymbol{\varepsilon}}_{\boldsymbol{p}} + \frac{\partial \psi}{\partial p}\dot{p} + \frac{\partial \psi}{\partial \beta}\dot{\beta} + s\dot{T}\right) \geq 0 \\ &= \boldsymbol{\sigma} : \dot{\boldsymbol{\varepsilon}}_{\boldsymbol{p}} - R\dot{p} + R\dot{\beta} \geq 0.\end{aligned} \tag{7}$$

where $\dot{\Phi}$ and $\dot{W}_\varepsilon$ denote, respectively, the rate of dissipated energy and the rate of strain energy. Therefore, the evolution of the internal state variables must be written in accordance with the above inequality to guarantee that the proposed constitutive model is well thermodynamically consistent.

2.2.1. Evolution of the plasticity-related variables

As usual in associative plasticity, the evolution of the hardening variable p and the plastic strain $\boldsymbol{\varepsilon}_p$ are governed by the normality rule of the yield function f, which also activate the plastic multiplier λ through the Kuhn-Tucker conditions:

$$f(\boldsymbol{\sigma}, R) = \mathrm{eq}(\boldsymbol{\sigma}) - R - R_0 \leq 0, \qquad \begin{cases} f < 0, & \dot{\lambda} = 0 \\ f = 0, & \dot{\lambda} > 0 \end{cases}, \tag{8}$$

where R_0 is the initial yield threshold. Thus, one obtains for the plasticity-related evolution equations:

$$\dot{p} = -\frac{\partial f}{\partial R}\,\dot{\lambda} = \dot{\lambda}, \qquad \dot{\boldsymbol{\varepsilon}}_{\boldsymbol{p}} = \frac{\partial f}{\partial \boldsymbol{\sigma}}\,\dot{\lambda} = \boldsymbol{\Lambda}(\boldsymbol{\sigma})\,\dot{p}, \tag{9}$$

where $\boldsymbol{\Lambda}(\boldsymbol{\sigma})$ denotes the plastic strain flow, given by:

$$\boldsymbol{\Lambda}(\boldsymbol{\sigma}) = \frac{\partial f}{\partial \boldsymbol{\sigma}} = \frac{3}{2}\frac{\mathbf{Dev}(\boldsymbol{\sigma})}{\mathrm{eq}(\boldsymbol{\sigma})}. \tag{10}$$

It is recalled that the convexity of f with regard to the associated variables $\boldsymbol{\sigma}$ and R ensures that the plasticity-related dissipation is always positive or null, i.e. $\boldsymbol{\sigma} : \dot{\boldsymbol{\varepsilon}}_{\boldsymbol{p}} - R\dot{p} \geq 0$.

2.2.2. Evolution of the hardening recovery variable

It is important to have in mind that achieving quantitative characterization of the recovery phenomenon remains very complicated and that there is no consensus regarding its evolution (Friedel, 1964; Humphreys, 2017). However, Petkovic et al. (1979) and Farzadi (2015) brought out that the recovery kinetic is mainly governed by the temperature and the dislocation density, where both act as driving forces for the recovery mechanism. Based on experimental trends observed in the above-mentioned references, a specific evolution law is proposed in this work to describe the kinetic of the recovery variable β. According to this law, the recovery rate is defined as the product of two sub-functions, which respectively represent the effects of the temperature and the dislocation density on the recovery kinetic. This gives:

$$\dot{\beta} = g(T) \times h(p - \beta). \tag{11}$$

The first sub-function, denoted by g, depends only on the temperature. This function is chosen under the form of a power law of the positive part[1] of the difference between the current and the activation temperature, T_a:

$$g(T) = A_T \langle T - T_a \rangle_+^{A_L}, \tag{12}$$

[1]The positive part of a scalar quantity a is denoted by $\langle a \rangle_+$, such that $\langle a \rangle_+ = a$ if $a \geq 0$ and $\langle a \rangle_+ = 0$ if $a < 0$.

where A_T and A_L are material parameters. T_a represents the temperature threshold from which the hardening recovery mechanism becomes active[2]. The second sub-function, denoted by h, depends on the difference between the hardening and the recovery variables (p and β), whose value is implicitly related to the current dislocation density. This function is chosen under the following exponential form:

$$h(p-\beta) = 1 - \exp\left(-\frac{p-\beta}{A_r}\right). \tag{13}$$

With this form, h is nearly equal to 1 when the value of β is far lower than the current value of p. In this case, the recovery rate is mainly influenced by the temperature through the sub-function g. However, h gradually goes to 0 when β approaches the current value of p. In this case, the recovery rate decreases and tends to zero, which prevents β to exceed p. Thus, the role of the sub-function h is to ensure that the material cannot restore more hardening than it has been generated. Note that the parameter A_r controls the influence of the remaining hardening to recover $(p-\beta)$ on the recovery rate. If A_r is small, then, at fixed temperature, the hardening recovery rate will start decreasing just before the full recovery. On the contrary, if A_r is large, then the recovery rate will be slowly decreasing long before the full recovery. Both types of evolution have been reported in various experimental studies (Petkovic et al., 1979; Vandermeer and Rath, 1990; Farzadi, 2015).

[2]Note that, experimental observations reported that slowly evolving recovery may exist at low temperatures (Orowan, 1940; Messerschmidt et al., 2010; Pham et al., 2015). In the present model, the activation temperature T_a may be interpreted as the threshold from which the recovery mechanism becomes significantly active on the considered time-scale.

The recovery kinetic in equation (11) is furthermore illustrated in Figure 1.

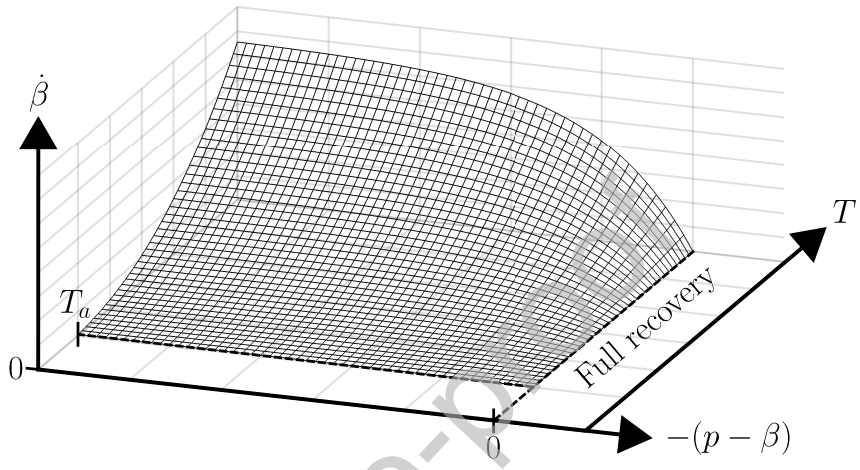

Figure 1: Schematic representation of the recovery kinetic: recovery rate ($\dot{\beta}$) vs. difference between the hardening and the recovery variable ($p-\beta$) vs. temperature (T).

It is worth noticing that, since R and $\dot{\beta}$ are necessarily positive, the hardening recovery-related dissipation is always positive or null, i.e. $R\dot{\beta} \geq 0$. Therefore, the proposed constitutive relation is thermodynamically allowable, according to equation (7).

2.3. Temperature field equation

The temperature field equation, commonly called heat equation, is obtained from the 1^{st} law of thermodynamics in which the expression of the Helmholtz free energy potential is substituted (Lemaître and Chaboche, 1990; Chatzigeorgiou et al., 2018; Praud, 2018), as detailed in Appendix A. For

the proposed model, after proper calculation (see Appendix A), this gives:

$$\rho c_p \dot{T} = -\mathrm{div}_{\boldsymbol{x}}(\boldsymbol{q}) + \omega + \underbrace{\dot{\Phi} - T\alpha \boldsymbol{I} : \dot{\boldsymbol{\sigma}}}_{\omega_\varepsilon}. \tag{14}$$

In the above equation, c_p denotes the heat capacity at constant pressure. $\boldsymbol{q}$ is the heat flux, classically defined for an isotropic material by:

$$\boldsymbol{q} = -k\ \mathbf{grad}_{\boldsymbol{x}}(T), \tag{15}$$

where k is the conductivity. ω stands for an eventual prescribed heat source. Note that, in the context of welding process simulation, the heat source ω may be utilized to represent the thermal load induced by a weld bead, although an external heat flux or a fixed temperature may be also considered in this purpose (Eagar and Tsai, 1983; Goldak et al., 1984; Seleš et al., 2018). ω_ε represents the internal heat produced by the mechanical work. The first and second terms of ω_ε depict the dissipation, already given in equation (7), and the thermomechanical coupling sources.

From equation (14), it is obvious that the deformation process of the material influences the temperature field equation through the internal heat produced by the mechanical work ω_ε. Therefore, rigorously, the unknown displacements and temperature must be solved as fully coupled fields. This is generally achieved through a fully coupled thermomechanical analysis, where the equilibrium equations (mechanical problem) and the heat equation (thermal problem) are simultaneously solved, while integrating all the coupling terms. However, the high temperatures involved with the welding process are significantly larger than the ones generated by the mechanical work. In

these conditions, the heat generated by the mechanical work, ω_ε, can be reasonably neglected in the temperature field equation (14), i.e. $\omega_\varepsilon \approx 0$. With this assumption, the temperature field equation becomes insensitive to the deformation of the material. Thus, the whole problem can be treated with an uncoupled thermomechanical analysis, where the thermal problem is solved prior to the mechanical one. The temperature field computed from the thermal analysis is then utilized as input data for the subsequent mechanical analysis. The simulations presented in this work were performed in this context.

2.4. Numerical implementation

The proposed constitutive model is implemented into the FE solver *ABAQUS/Standard* with the help of a User Material subroutine (UMAT). The numerical integration algorithm is based on the *convex cutting plane* form of the *return mapping algorithm* (Simo and Ortiz, 1985; Ortiz and Simo, 1986; Simo and Hughes, 1998; Praud et al., 2017a,b) and is detailed in Appendix B.

As explained in the previous section, uncoupled thermomechanical analyses are considered in this work. Thus, the temperature field is first computed from a thermal analysis and is next set as input data for the mechanical analysis, in which the UMAT is utilized.

3. Experimental identification

3.1. Experimental procedure and testing

In this section, it is proposed to apply the previously formulated constitutive model to study the hardening recovery of an austenitic 316L stainless steel alloy. To do so, an experimental program involving uniaxial compressive tests and annealing treatments, was conducted to highlight the hardening recovery phenomenon occurring near weld beads during the welding process. It is assumed that high temperatures with high heating kinetics is reached near weld beads, whereas, far from them, temperatures and heating kinetics are lower (Murugan et al., 1998). This is why heat treatments should be carefully chosen to simulate the range of temperature and heating kinetics seen by the welded part near weld beads.

The compressive tests were conducted on four cylindrical samples named S1, S2, S3 and S4, coming from a hot wire drawing rod. Their dimensions are 10 mm in diameter and 24 mm in length. Prior to the tests, all samples have undergone a stress-released heat treatment at 950°C during 40 min at 1 bar in air, to remove residual stresses induced prior the forming process and sample preparation. The compressive tests were realized at room temperature, $T_{room} = 293.5$ K, with the help of a hydraulic ZWICK 100 kN, monitoring the uniaxial stress (σ_{11}) with a load cell (Figure 3a). A MultiXtens extensometer has been used for the uniaxial strain measurement (ε_{11}), considering an initial gauge length of 15 mm. A constant nominal strain rate of 5×10^{-4} s^{-1} was piloted by moving cross-head for all samples. Then, the following thermomechanical loading configurations were performed:

- Thermomechanical loading path for S1 sample:

  Sample S1 was first subjected to a compressive strain of 0.035 (step 1: loading), before being unloaded and left free of stress (step 2: unloading). The sample was next heated up to a maximum temperature T_{max} (step 3: heating) and cooled down to room temperature T_{room} while being kept free of stress (step 4: cooling). Then, the sample was subjected to another compressive strain of 0.035 (step 5: loading), before being one more time unloaded and left free of stress (step 6: unloading). This thermomechanical loading path is illustrated in Figure 2a. During this test, the heat treatment (steps 3 and 4) was conducted under vacuum at 4×10^{-5} mbar on a NETZCH dilatometer with a radiative heating system. The temperature was recorded with a S thermocouple in contact with the sample. Both the heating and cooling stages were controlled during the test.

- Thermomechanical loading path for S2, S3, and S4 samples:

  Samples S2, S3 and S4 were first subjected to a compressive strain of 0.035 (step 1), before being unloaded and left free of stress (step 2). The samples were next heated up to a maximum temperature T_{max} at fixed strain (step 3), unloaded to zero stress at fixed temperature (step 4) and cooled down to room temperature T_{room} while being kept free of stress (step 5). Then, the sample is subjected to another compressive strain of 0.035 (step 6), before being one more time unloaded and left free of stress (step 7). This thermomechanical loading path is illustrated in Figure 2b. During these tests, the heat treatments (steps 3, 4 and 5)

were performed on a GLEEBLE machine with inductive heating system (Figure 3b) at atmospheric pressure with argon used as shielding gas. The temperature was recorded with a K thermocouple directly welded on the sample. During the heat treatment (steps 3, 4 and 5), it is important to mention that the stress was technically not measurable during the heating stage (step 3), which occurred at fixed strain. Next, during the following unloading and cooling stages (steps 4 and 5), where the stress was released and left free, the strain was also technically not measurable. Nonetheless, the strain at the beginning of the second loading stage (step 6) was evaluated by measuring the samples before and after the heat treatment. During these tests, the heating stage (step 3) was temperature-controlled, while the cooling stage (step 5) was free to T_{room}.

For each sample, the details of the heat treatments in terms of maximum temperature and heating/cooling kinetics are summarized in Table 1.

Table 1: Details of the heat treatments for S1, S2, S3 and S4 samples.

Sample	S1	S2	S3	S4
T_{max} (K)	673	973	1273	1423
Heating rate (K.s^{-1})	0.7	70	333.3	383.3
Time held at T_{max} (s)	10	1	1	5
Cooling rate (K.s^{-1})	0.3	free	free	free

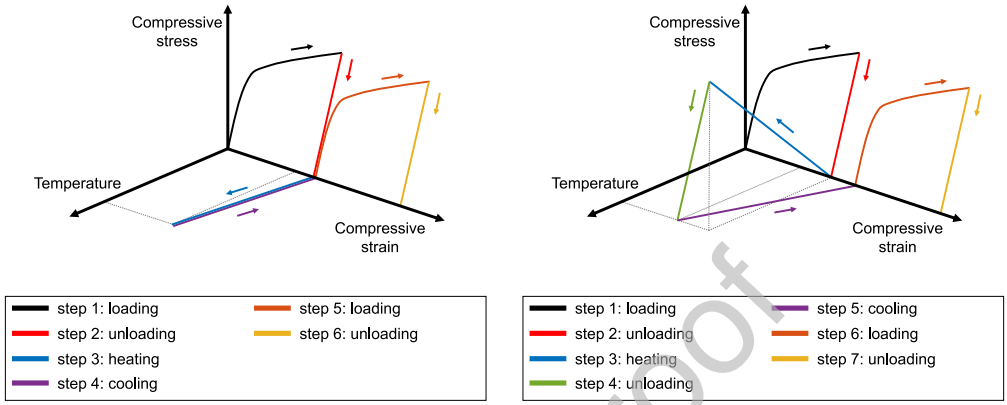

(a) Thermomechanical loading path for S1

(b) Thermomechanical loading path for S2, S3 and S4

Figure 2: Experimental thermomechanical loading paths.

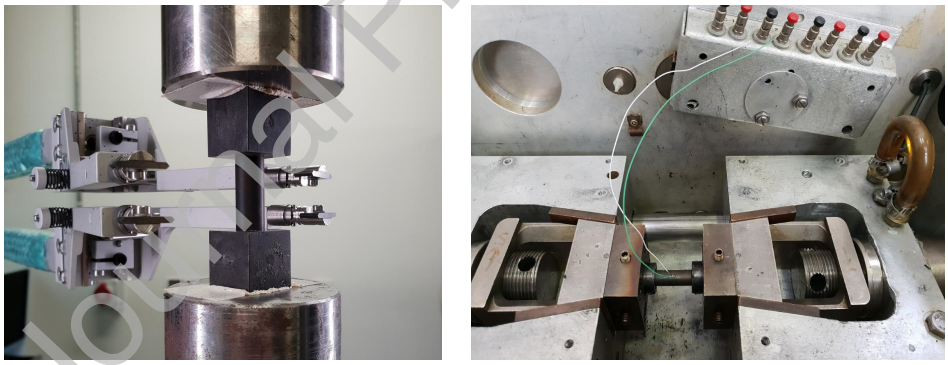

(a) Compressive test on Zwick machine

(b) Heat treatment on Gleeble machine

Figure 3: Experimental set-up for the thermomechanical tests.

It is worth noticing that, for the first thermomechanical loading path (for sample S1), the heat treatment was performed under free stress conditions, leaving the material free to expand and to contract. Therefore, the material

exhibits a static recovery, as the hardening recovery phenomenon occurred independently from the plasticity. Such a configuration is particularly convenient for the identification of the model parameters. However, the equipment at our disposal (NETZCH dilatometer with radiative heating system) allows to realize heat treatments under free stress conditions only for moderate temperatures (≈1000°C), which appear to be lower than the recovery activation temperature. This is why only S1 sample was tested with this configuration.

To overcome this issue, the second thermomechanical loading path was realized for samples S2, S3 and S4 with another equipment (GLEEBLE machine with inductive heating system) allowing to perform heat treatments in a higher temperature range but only at fixed strain for the heating stage. Under these conditions, the material cannot freely expand and the compressive stresses were generated into the sample, which may potentially plastify during the heating stage. Therefore, the material can exhibit a dynamic recovery. Since the elasto-plastic properties are assumed to be temperature-independent in the present model, which may not be the case in reality, the dynamic recovery conditions are not ideal for the identification of the model parameters. Nevertheless, in the context of this first study, these tests will be utilized for the parameter identification of the proposed model.

3.2. Identification of the parameters

The parameters of the proposed constitutive model were identified from the experimental tests previously introduced.

For sample S1, the maximum temperature T_{max} appears to be not high

enough to activate the recovery mechanism. Therefore, this test can be utilized to identify the plasticity parameters R_0, Q_1, Q_2 and b through standard procedures for plastic materials (Lemaître and Chaboche, 1990). The coefficient of thermal expansion α, is directly determined from the dilatometer measurements during the heat treatment. The obtained parameters are listed in the upper part of Table 2. The experimental data for this test are compared to the computed material response in Figure 4.

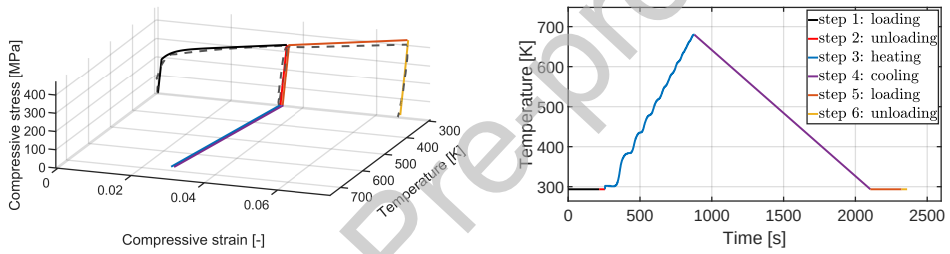

(a) Stress (σ_{11}) vs. strain (ε_{11}) vs. temperature (T) for sample S1

(b) Temperature (T) vs. time for sample S1

Figure 4: Thermomechanical test for the S1 sample. In Figure 4a, the dashed line depicts the experimental material's response, while solid lines represent the response computed by the model using the experimentally measured temperature in Figure 4b. The color code of the steps is the same as Figure 2a and is recalled in Figure 4b.

The hardening recovery parameters were next identified from the experimental data coming from samples S2, S3 and S4. Then, the parameters T_a, A_T, A_L, A_r were identified using a reverse engineering algorithm based on the Levenberg-Marquardt technique (Levenberg, 1944; Marquardt, 1963; Meraghni et al., 2014). This method consists in adjusting the unknown model parameters by minimizing a cost function generally expressed by the least

squares between the computed response and the experimental data. It is recalled that the material response is not measured during the heat treatment (steps 3, 4 and 5). Thus, the identification was carried out only on the loading and unloading stages (steps 1, 2, 6 and 7). The obtained parameters are listed in the lower part of Table 2. Comparisons between the experimental data and the computed material responses are presented in Figure 5 for samples S2, S3 and S4.

Table 2: Identified material parameters for austenitic 316L stainless steel alloy.

Feature	Parameter	value	unit
Elasticity	E	193500	MPa
	ν (standard value)	0.3	-
Thermal expansion	α	17.1×10^{-6}	K^{-1}
	T_0	293.5	K
Plasticity	R_0	190	MPa
	Q_1	50	MPa
	b	400	-
	Q_2	2880	MPa
Hardening recovery	T_a	673.5	K
	A_T	5×10^{-7}	$K^{-A_L}.s^{-1}$
	A_L	2.5	-
	A_r	40	-

For sample S1 (see Figure 4), as previously mentioned, the maximum

temperature reached throughout the heat treatment was not high enough to activate the hardening recovery mechanism. Thus, at the beginning of the second loading stage, the hardening was approximately at the same level as the one reached at the end of the first loading stage.

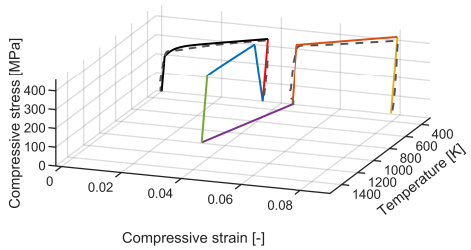

(a) Stress (σ_{11}) vs. strain (ε_{11}) vs. temperature (T) for sample S2

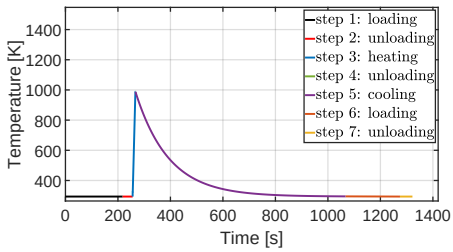

(b) Temperature (T) vs. time for sample S2

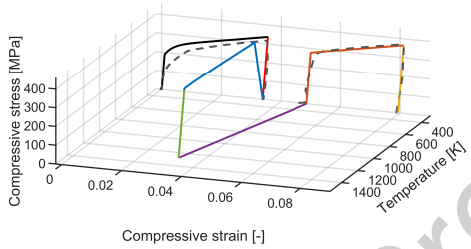

(c) Stress (σ_{11}) vs. strain (ε_{11}) vs. temperature (T) for sample S3

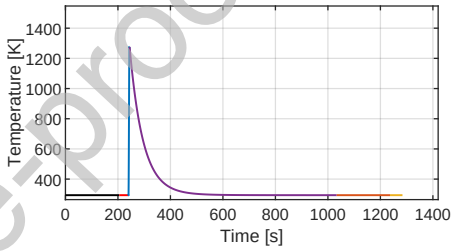

(d) Temperature (T) vs. time for sample S3

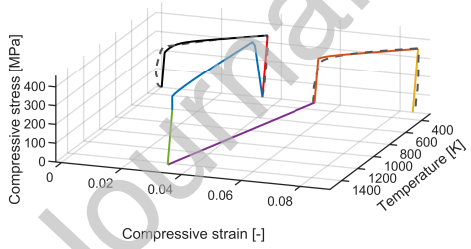

(e) Stress (σ_{11}) vs. strain (ε_{11}) vs. temperature (T) for sample S4

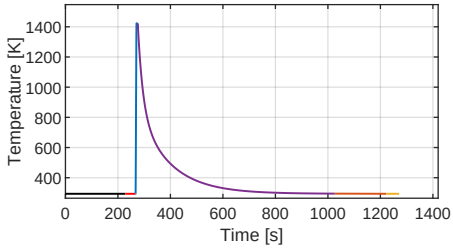

(f) Temperature (T) vs. time for sample S4

Figure 5: Thermomechanical tests for samples S2, S3 and S4. In Figures 5a, 5c and 5e, dashed lines depict the experimental material's response, while solid lines represent the response computed by the model using the experimentally measured temperatures in Figures 5b, 5d and 5f, respectively. The color code of the steps is the same as Figure 2b and is recalled in Figure 5b. Note that, since the step 4 (the second unloading) occurs quasi-instantaneously, the corresponding green colored line is not visible in Figures 5b, 5d and 5f, but is well present between the blue and purple colored lines.

For samples S2, S3 and S4 (see Figure 5), the material responses were overall well captured during the first loading and unloading stages (steps 1 and 2). However, it is worth noticing that there is a slight shift between the experiment and the computed response for sample S3 (see Figure 5c). Moreover, one can remark a small tensile (negative compressive) strain in the experimental data for sample S4 (Figure 5e) during the first loading stage (step 1). This may come from an unsuitable parallelism of the sample's faces, which might have induced small perturbations of the strain measurement at the beginning of the compression. During the heating stage (step 3), which occurred at fixed strain, compressive stress was generated as the material cannot freely expand. The generated stress levels appeared to be important enough to cause plastic flow with hardening. During this stage the hardening recovery also became active as the temperature increased and exceeded the activation threshold of this mechanism (T_a). This produced a small stress drop at the end of the heating stage (step 3), which can be clearly observed on sample S4 (see Figure 5e), whereas it is barely visible for sample S2 and S3 (see Figures 5a and 5c). Next, the material was quasi-instantaneously unloaded to zero stress (step 4) and left free of stress during the following cooling stage (step 5), during which the sample could freely shrink. After returning at room temperature, the second loading stage was carried out (step 6) with an associated stress response reflecting the partial or full recovery. The temperature reached during the heat treatment of sample S4 was high enough and permitted the material to recover most of its hardening. For samples S2 and S3, the intermediate temperatures produced a partial hardening recovery of the material.

The overall good agreement between the computed results and the experimental data demonstrated the capabilities of the model to capture the thermomechanical response of metallic materials exhibiting thermally-activated hardening recovery.

4. Numerical simulations

4.1. Thermomechanical response of a material point

In this section, additional examples are presented to provide a better understanding of the proposed model, as well as to illustrate its predictive capabilities. These examples were carried out on a single material point under uniaxial loading conditions with the material parameters listed in Table 2.

4.1.1. Example 1: Study of static recovery

In this first example, the material was loaded up to a stress level of 300 MPa in 100 s before being fully unloaded in another 100 s. During this stage, the temperature was kept constant and equaled to the reference temperature ($T_0 = 293.5$ K). The material was next left free of stress for 100 s, during which the temperature was raised to a maximum value T_{max} in 100 s before returning to the reference temperature T_0 in another 100 s. In the last stage, the material was reloaded up to 350 MPa under constant temperature. Assuming a melting temperature T_m for 316L of 1773 K, three values of T_{max} were considered: 573.5 K ($0.3 \times T_m$), 1073.5 K ($0.6 \times T_m$) and 1473.5 K ($0.8 \times T_m$). The first one was lower than the activation temperature T_a, the second one was slightly greater than T_a, whereas the third one was much

greater than T_a. These thermomechanical loading paths are illustrated in Figure 6.

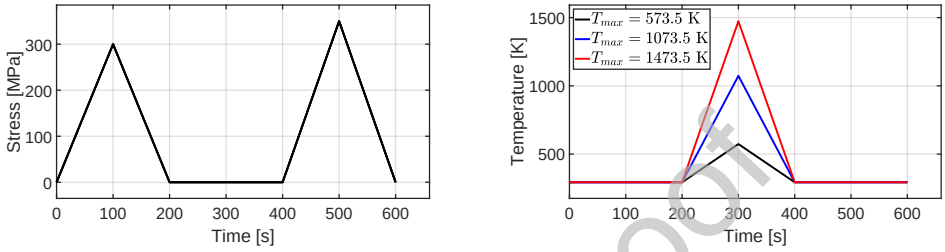

(a) Applied stress (σ_{11}) vs. time

(b) Applied temperature (T) vs. time

Figure 6: Example 1: Applied thermomechanical loading paths in the case of static recovery.

This example highlights the effect of the thermally-activated hardening recovery on the thermo-elasto-plastic response of the material in the case of static recovery, when the plasticity and the hardening recovery are separately activated. The results of these simulations are presented in Figure 7. Plastic strain and hardening were generated during the first loading stage. When the material was next heated under free stress conditions, there was no hardening recovery if the temperature does not exceed T_a (see Figure 7b). Thus, at the next reloading stage, the material started plastifying from the previously reached stress level (see Figure 7a). However, if the temperature exceeded T_a, then the hardening could gradually recover (see Figures 7d and 7f). In this case, during the reloading stage, the material started plastifying from a stress level lower than the one previously reached (see Figures 7c and 7e). The hardening may be partially or fully recovered, depending on the

temperature reached and the time the material has been kept at this temperature (see Figures 7c, 7d , 7e and 7f).

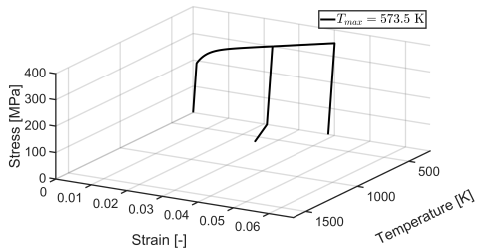

(a) Stress (σ_{11}) vs. strain (ε_{11}) vs. temperature (T) for $T_{max} = 573.5$ K

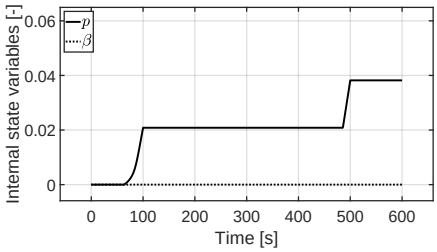

(b) Hardening and recovery variables (p and β) vs. time for $T_{max} = 573.5$ K

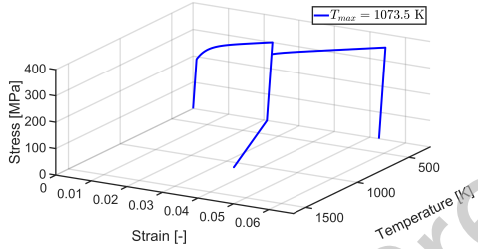

(c) Stress (σ_{11}) vs. strain (ε_{11}) vs. temperature (T) for $T_{max} = 1073.5$ K

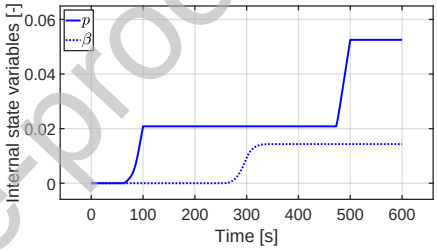

(d) Hardening and recovery variables (p and β) vs. time for $T_{max} = 1073.5$ K

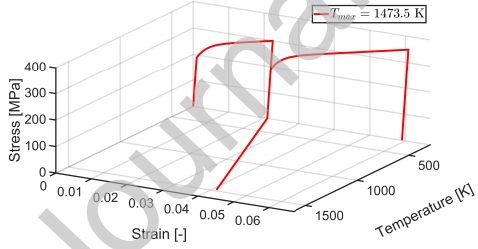

(e) Stress (σ_{11}) vs. strain (ε_{11}) vs. temperature (T) for $T_{max} = 1473.5$ K

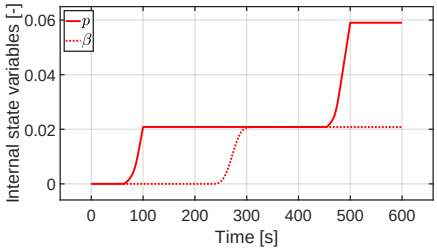

(f) Hardening and recovery variables (p and β) vs. time for $T_{max} = 1473.5$ K

Figure 7: Example 1: Simulated material responses in the case of static recovery. This example illustrates the cases of non-recovery, partial recovery and full recovery of the hardening according to the temperature levels reached.

4.1.2. Example 2: Study of dynamic recovery under monotonic loading

In the second example, the material was, in a first step, left free of stress while the temperature was elevated up to certain level T_{max} hold for 5 s. During this stage the material could freely expand. The same values of T_{max} as for the first example were considered, namely: 573.5 K, 1073.5 K and 1473.5 K. In a second time, a strain of 0.05 was applied with a strain rate of 5×10^{-4} s^{-1}, while the temperature was kept constant. An additional case with a higher strain rate: 5×10^{-3} s^{-1} was also considered for $T_{max} = 1073.5$ K. These thermomechanical loading paths are illustrated in Figure 8.

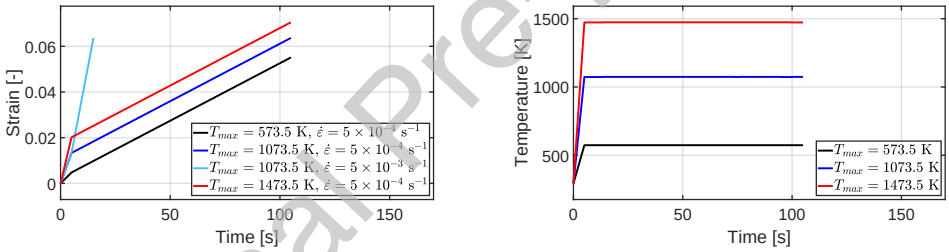

(a) Applied strain (ε_{11}) vs. time (b) Applied temperature (T) vs. time

Figure 8: Example 2: Applied thermomechanical loading paths in the case of dynamic recovery under monotonic loading.

This example highlights the effect of the thermally-activated hardening recovery on the thermo-elasto-plastic response of the material in the case of dynamic recovery, when the plasticity and the hardening recovery are simultaneously activated, under monotonic loading. The results of these simulations are presented in Figures 9 and 10. If the temperature of the material did not exceed T_a, the simulation indicated that the hardening recovery was

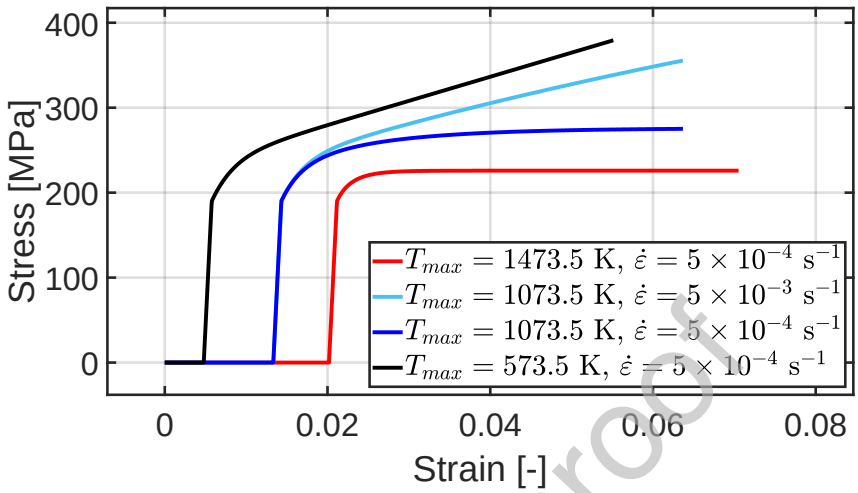

Figure 9: Example 2: Simulated material responses, stress (σ_{11}) vs. strain (ε_{11}), in the case of dynamic recovery under monotonic loading.

not active (see Figure 10a) and the material response corresponds to the one of a classical plastic model (see the black curve in Figure 9). However, if the temperature exceeded T_a, then the hardening started to be recovered at the same time than it was generated (see Figures 10b, 10c and 10d). If the temperature was high enough, then the hardening was recovered almost as fast as it was generated (see Figure 10d), making the material response quasi similar to a perfectly plastic material (see the red curve in Figure 9). At lower temperatures, the hardening was generated much faster than it was recovered (see Figures 10b and 10c), leading to an intermediate response between the two previous cases (see dark and light blue curves in Figure 9). This intermediate response appears to be time-dependent as the latter is sensitive to the applied strain rate (see dark and light blue curves in Figure 9). Indeed, although the plasticity-related evolution laws are time-independent (see Sec-

tion 2.2.1), the one related to the hardening recovery is time-dependent (see Section 2.2.2), which makes the overall material response time-dependent when both mechanisms are active.

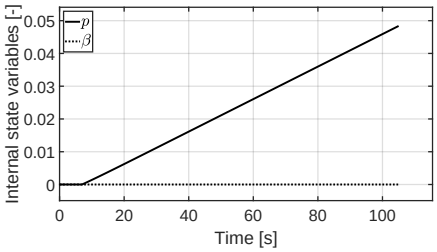

(a) Hardening and recovery variables (p and β) vs. time for $T_{max} = 573.5$ K and $\dot{\varepsilon} = 5 \times 10^{-4}$ s^{-1}

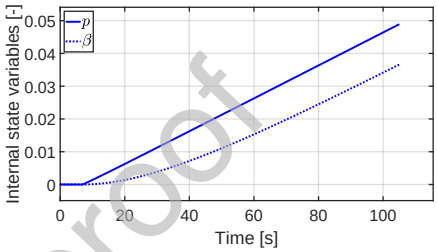

(b) Hardening and recovery variables (p and β) vs. time for $T_{max} = 1073.5$ K and $\dot{\varepsilon} = 5 \times 10^{-4}$ s^{-1}

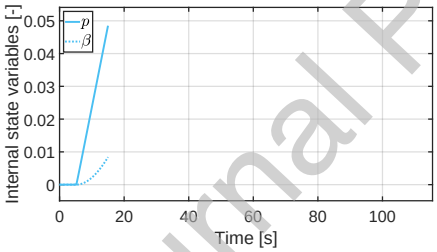

(c) Hardening and recovery variables (p and β) vs. time for $T_{max} = 1073.5$ K and $\dot{\varepsilon} = 5 \times 10^{-3}$ s^{-1}

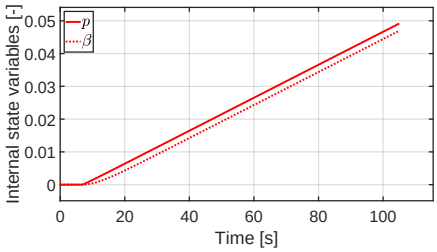

(d) Hardening and recovery variables (p and β) vs. time for $T_{max} = 1473.5$ K and $\dot{\varepsilon} = 5 \times 10^{-4}$ s^{-1}

Figure 10: Example 2: Evolution of the internal state variables p (hardening variable) and β (recovery variable), in the case of dynamic recovery under monotonic loading.

4.1.3. Example 3: Study of dynamic recovery-induced stress relaxation

In the third example, a strain of 0.01 was applied at the reference temperature (T_0 = 293.5 K) in 5 s. In a second stage, the stress reached after the previous loading was kept constant, the material was heated up to a certain temperature T_{max} in 5 s, and left free to expand. Then, the strain and temperature were both kept constants. The same values of T_{max} as for the first example were considered, namely: 573.5 K, 1073.5 K and 1473.5 K. These thermomechanical loading paths are illustrated in Figure 11.

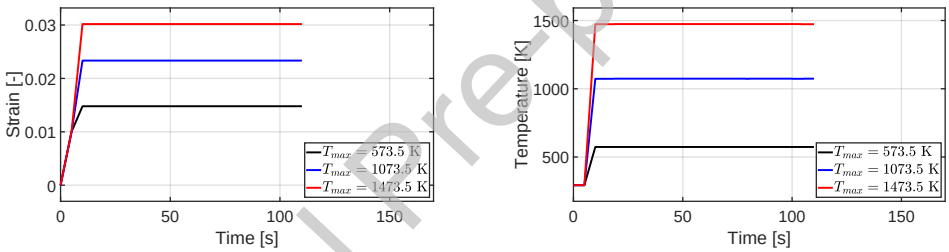

(a) Applied strain (ε_{11}) vs. time (b) Applied temperature (T) vs. time

Figure 11: Example 3: Applied thermomechanical loading paths in the case of dynamic recovery-induced stress relaxation.

This example highlights the stress relaxation induced by a dynamic recovery under constant strain. The results of these simulations are presented in Figure 12. When the material was heated up above the activation temperature T_a, the hardening recovery became active under constant strain. Therefore, due to the gradually decreasing yield stress, the material plastified, leading to an apparent stress relaxation. The higher the temperature, the faster is the recovery rate and thus the relaxation (see blue and red curves

in Figure 12). However, if the temperature did not exceed T_a, the recovery remained inactive and the material did not undergo any relaxation (see black curve in Figure 12). It is noted that, according to the model formulation, the stress cannot decrease beyond the yield threshold R_0 during the relaxation.

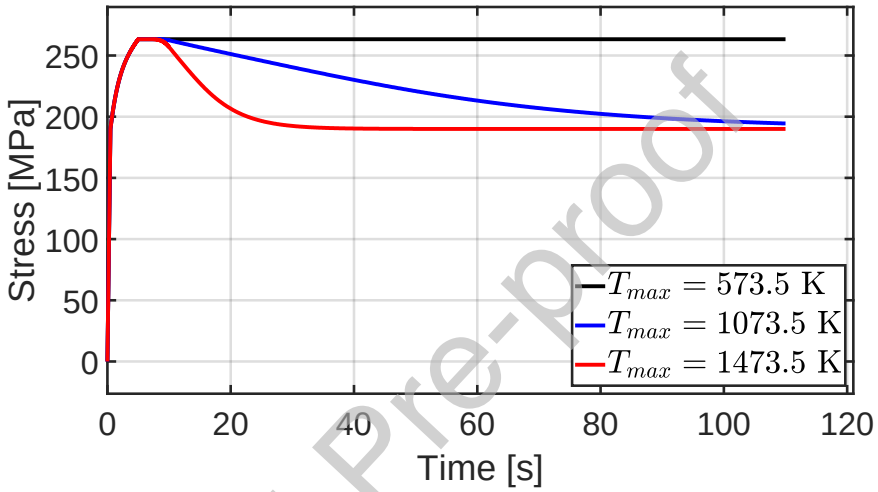

Figure 12: Example 3: Simulated material responses, stress (σ_{11}) vs. time, in the case of dynamic recovery-induced stress relaxation.

4.2. Three-dimensional FE application

The capabilities of the proposed model in the context of welding applications are illustrated through an example of a clamped plate locally heated at its center representing the thermal load induced by a weld bead (see Figure 13). The dimensions of the plate, as well as the thermal and mechanical boundary conditions applied on it are shown in Figure 13a. Due to symmetries, only one fourth of the plate is represented and appropriate boundary conditions were applied on the planes of symmetry. Zero displacements are

set to the clamped face on which adiabatic conditions are assumed. All the other external surfaces of the plate were subjected to convective boundary conditions, that were active during the whole analysis, considering an exchange coefficient $H = 10 \times 10^{-3}$ mW.mm^{-2}.K^{-1} and an constant external temperature $T_\infty = T_0 = 293.5$ K, which was also equal to the initial temperature of the system. The plate was locally heated at the center of its top face, on a small band area on which a heat flux q was applied. As shown in Figure 13b, this heat flux q was initially null before taking the value of 4×10^3 mW.mm^{-2} during the heating stage, which lasted from $t = 100$ s to $t = 200$ s. Afterwards came the cooling stage, where q was set back to zero until the end of the analysis, at $t = 3800$ s. The plate was made with the same material as the one identified in section 3, namely: 316L austenitic stainless steel alloy, whose parameters and thermal properties are listed in Tables 2 and 3, respectively.

The FE mesh contained 23664 nodes and 20691 first order hexaedral solid elements (see Figure 13c). As explained in Section 2.3, it was assumed the thermal problem was not influenced by the mechanical one. Hence, the thermal problem was solved in a first stage and the obtained temperature field was set as an input for the mechanical analysis to be solved in a second stage. Note that the same mesh was used for both analyses.

The results of the thermal analysis are shown in Figure 14. During the heating stage, the temperature rapidly increased and diffused from the center of the plate top face, where the heat flux was applied. During the subsequent cooling stage, the plate was not heated anymore, thus the temperature grad-

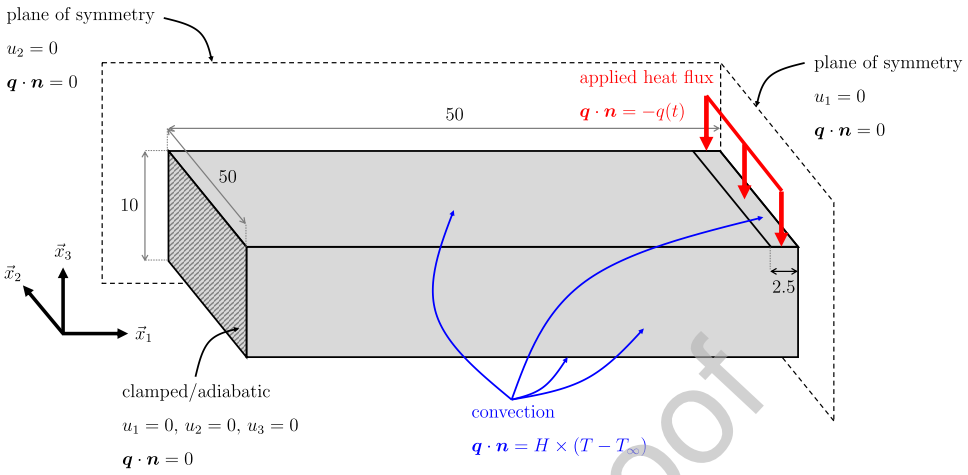

(a) Dimension (in mm) of the plate and thermomechanical boundary conditions

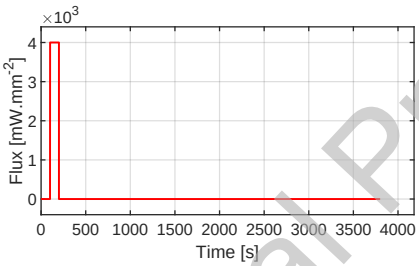

(b) Applied heat flux (q) vs. time

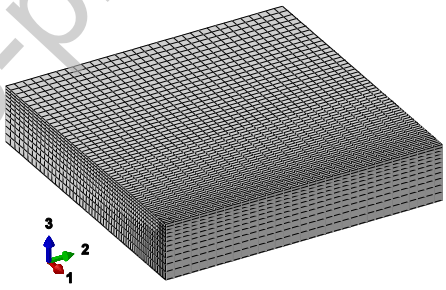

(c) FE mesh of the plate

Figure 13: Three-dimensional FE application: clamped plate locally heated at its center.

ually returned to the external temperature T_∞ as the heat was extracted by convection with the external environment. In this example, the attention will be focused on three points A, B and C (see Figure 14a), where the levels of stress, plasticity and recovery will be analyzed. The Point A was located relatively far away from the heated area, the Point B lied in the vicinity of the heated area, while the Point C was in the heated area. The highest temperatures reached at points A, B and C were of 665.2 K, 991.0 K and

Table 3: Thermal properties for austenitic 316L stainless steel alloy (Depradeux, 2004).

Feature	Parameter	value	unit
Mass density	ρ	8×10^{-9}	$\mathrm{T.mm^{-3}}$
Heat capacity	c_p	577.3×10^{6}	$\mathrm{mJ.T^{-1}.K^{-1}}$
Thermal conductivity	k	21.3	$\mathrm{mW.mm^{-1}.K^{-1}}$

1731.5 K, respectively (see Figure 14b).

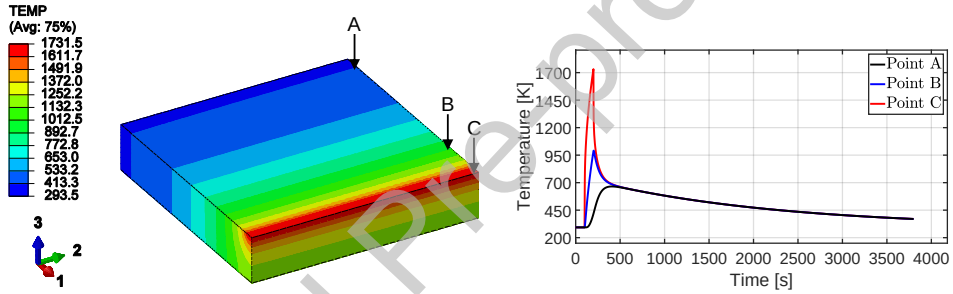

(a) Temperature field (T) at the end of the heating stage ($t = 200$ s)

(b) Temperature (T) vs. time at points A, B and C

Figure 14: Three-dimensional FE application: temperature field computed from the thermal analysis.

The results of the mechanical analysis are presented in Figures 15 and 16. Figures 15a and 15b displays the spatial distribution of the Von Mises stress eq($\boldsymbol{\sigma}$) across the plate at the end of the heating stage ($t = 200$ s) and at the end of the analysis ($t = 3800$ s), respectively. Figures 16a, 16c and 16e show, at points A, B and C, the evolution of the the Von Mises stress eq($\boldsymbol{\sigma}$), along with the hydrostatic stress hyd($\boldsymbol{\sigma}$) in order to visualize whether tension (hyd($\boldsymbol{\sigma}$) > 0) or compression (hyd($\boldsymbol{\sigma}$) < 0) stresses were involved. In

addition, Figures 16b, 16d and 16f show the evolution of the hardening and recovery variables at points A, B and C, respectively.

During the heating stage, the plate overall entered in axial compression as its expansion was prevented along $\vec{x}_1$ (see Figures 16a, 16c and 16e). One can also notice some stress concentrations around the edge of the clamped surface due to prevented expansion along $\vec{x}_2$ (see Figure 15a). The induced

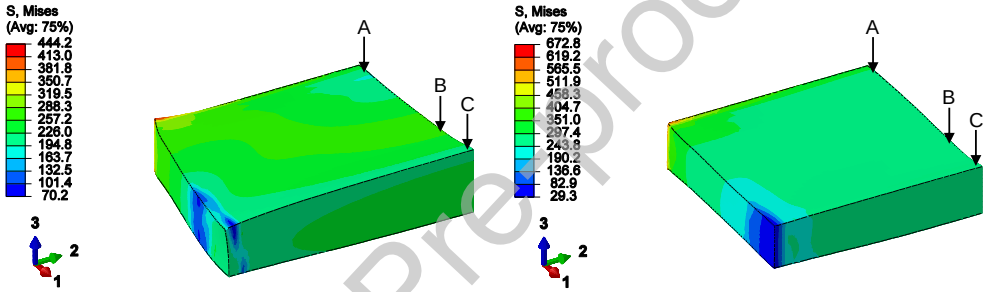

(a) Von Mises stress (eq($\boldsymbol{\sigma}$)) at the end of the heating stage ($t = 200$ s)

(b) Von Mises stress (eq($\boldsymbol{\sigma}$)) at the end of the analysis ($t = 3800$ s)

Figure 15: Three-dimensional FE application: Von Mises stress field computed from the mechanical analysis. The results are projected on the deformed configuration, which is amplified by a factor $\times 15$.

compressive stresses were overall sufficiently important so that plastic deformations could be generated. At the point A, which is away from the heated area, the maximum reached temperature (665.2 K) appeared to be too low to activate the hardening recovery and only a small amount of plastic deformations were generated (see Figure 16b). At the point B, which lies in the vicinity of the heated area, the maximum reached temperature was high enough (991.0 K) to activate the hardening recovery. At this point, about

50% of the generated hardening has been recovered (see Figure 16d). At the point C, which is in the heated area, the maximum reached temperature was much higher (1731.5 K). This led to an important hardening recovery, which even more promoted further plastic deformations. At this point, about 80% of the generated hardening has been recovered (see Figure 16f). During the cooling stage, the plate shrank (see Figure 15b) as the temperature gradually decreased and returned to the ambient temperature T_∞. Thus, the plate overall entered in axial tension with stress levels high enough so that plastic deformations are generated anew under tensile mode. However, the hardening recovery stopped evolving quickly as the temperature rapidly dropped below the activation threshold of this mechanism (see Figures 16b, 16d and 16f).

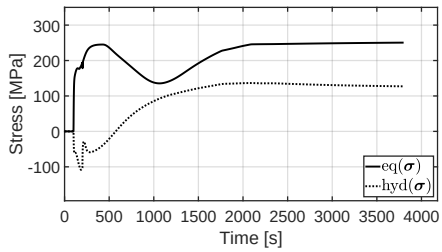

(a) Von Mises and hydrostatic stresses (eq($\boldsymbol{\sigma}$) and hyd($\boldsymbol{\sigma}$)) vs. time at point A

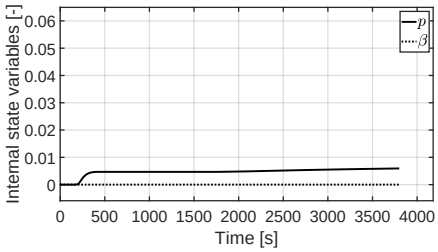

(b) Hardening and recovery variables (p and β) vs. time at point A

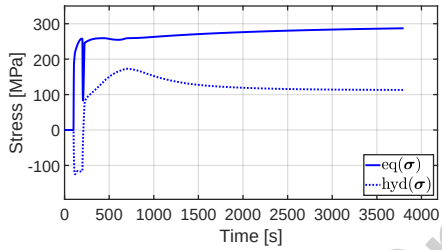

(c) Von Mises and hydrostatic stresses (eq($\boldsymbol{\sigma}$) and hyd($\boldsymbol{\sigma}$)) vs. time at point B

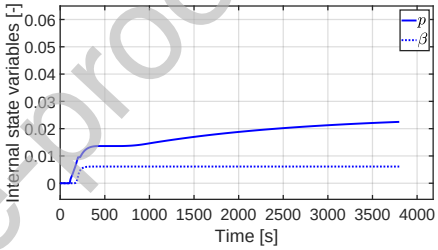

(d) Hardening and recovery variables (p and β) vs. time at point B

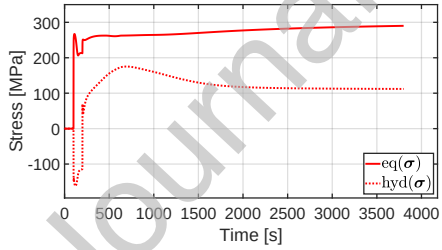

(e) Von Mises and hydrostatic stresses (eq($\boldsymbol{\sigma}$) and hyd($\boldsymbol{\sigma}$)) vs. time at point C

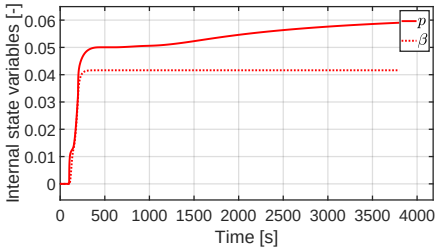

(f) Hardening and recovery variables (p and β) vs. time at point C

Figure 16: Three-dimensional FE application: Evolution of the Von Mises and hydrostatic stresses (eq($\boldsymbol{\sigma}$) and hyd($\boldsymbol{\sigma}$)), and internal state variables p (hardening variable) and β (recovery variable), at point A, B and C.

5. Discussion towards future improvements

As it is formulated, the elasto-plastic part of the model is temperature- and time-independent. However, it has been shown that temperature- and time-dependent effects arise from the hardening recovery mechanism. In reality, metallic materials are known to have elasto-plastic properties temperature-dependent and may also display time-dependent (viscoplastic) behavior at moderately high temperature before the activation of the recovery mechanism. For example, with the proposed model, the stress cannot decrease beyond the yield threshold during a relaxation induced by a dynamic recovery, whereas, experimentally, the stress is expected to vanish due to additional temperature- and time-dependent effects (Depradeux, 2004). Previous studies have also demonstrated that, in welding process, the value of yield threshold at high temperature has a small influence on the residual stresses, but a large effect on the prediction of residual distortions (Bru et al., 1996; Leblond et al., 1997; Bergheau et al., 2004). Long-time annealing involving recrystallization and grain growth may also modify the mechanical properties such as the shape of the hardening function (Chen et al., 2014). Taking into account the time- and temperature-dependencies may be substantial for the numerical simulation of welding process. Therefore these effects are intended to be integrated in the context of future improvements. For example, a temperature-dependent hardening function might be considered along with a viscoplastic or even a viscoelastic-viscoplastic formulation.

With the proposed model, the plastic deformation is governed by an isotropic hardening rule. Such a description is generally sufficient when

the material is exclusively subjected to tension or compression. However, during the welding process, the material may be alternately subjected to tension and compression. To treat such cases, it is also intended to extend the proposed concept of hardening recovery to kinematic and/or combined isotropic-kinematic hardening.

Integrating more complex temperature- and time-dependencies and kinematic hardening rules in the model would also require more-advanced characterization techniques. In this purpose, performing tension/compression tests at different strain-rates and temperatures would be useful to more clearly identify the contribution of the hardening recovery on the time- and temperature-dependent response of the material. The *Satoh* test could also be carried out (Satoh and Ohnishi, 1972). This thermomechanical test is generally well representative of all the phenomena occurring during the welding process (Mochizuki et al., 2002; Depradeux and Coquard, 2018).

6. Conclusions

In this work, a new thermodynamically-consistent modeling approach has been developed to describe the thermally-activated hardening recovery of thermo-elasto-plastic metals during annealing. The proposed constitutive equations consist in a classical thermo-elasto-plastic formulation, which is enhanced by an additional internal state variable, so-called *recovery variable*. The latter counteracts the effect of the hardening through a temperature-dependent evolution law.

An experimental program involving uniaxial compressive tests and heat treatments on a 316L austenitic stainless steel has been carried out to identify the model parameters. The good agreement between the experimental and computed results have demonstrated the capabilities of the model to capture the thermomechanical response of metallic materials exhibiting thermally-activated hardening recovery. Further simulations have been performed to provide a better understanding of the proposed model and to highlight the specific cases of static and dynamic recovery.

The proposed modeling approach is intended to be utilized for the simulation of welding process, to predict the reliability of welded engineering structures through the evaluation of residual stresses and distortions. In this context, future improvements are planned, like accounting for temperature-dependent elasto-plastic properties and/or extending the recovery mechanism to kinematic hardening rules.

Acknowledgments

This research was supported by Fives Cryo (Golbey, France) and Région Lorraine. We thank our colleagues P. Moll and L. Peltier from LEM3, Université de Lorraine, who provided expertise on experimental procedure and protocol that greatly assisted the research.

Appendix A. Relation with the temperature field equation

According to the 1^{st} law of thermodynamics, the rate of internal energy per unit of mass, e, in a material volume element, is equal to the sum of the power produced by this material (heat source ω) and its deformation (strain energy rate $\dot{W}_\varepsilon = \boldsymbol{\sigma} : \dot{\boldsymbol{\varepsilon}}$) minus the power leaving the material through the heat flux $\boldsymbol{q}$. This gives:

$$\rho\dot{e} = \omega + \dot{W}_\varepsilon - \mathrm{div}_{\boldsymbol{x}}(\boldsymbol{q}). \tag{A.1}$$

The Helmholtz ψ free energy potential is connected to the internal energy e and the entropy s by:

$$\psi = e - Ts, \tag{A.2}$$

or, in rate form:

$$\dot{\psi} = \dot{e} - (s\dot{T} + \dot{s}T). \tag{A.3}$$

Thus, inserting the (A.3) into (A.1) leads to the general expression of the heat equation:

$$\rho T\dot{s} = \omega + \underbrace{\dot{W}_\varepsilon - \rho(\dot{\psi} + s\dot{T})}_{\dot{\Phi}} - \mathrm{div}_{\boldsymbol{x}}(\boldsymbol{q}). \tag{A.4}$$

For the proposed model, the common form of the calorific energy term in the Helmholtz free energy potential is adopted:

$$\psi_0(T) = c_p\left((T - T_0) - T\ \ln\left(\frac{T}{T_0}\right)\right) - s_0\ (T - T_0) + e_0, \tag{A.5}$$

where s_0 and e_0 are respectively, the value of entropy and internal energy, at $T = T_0$, while c_p denotes the specific heat capacity at constant pressure.

Introducing the above definition in equation (1), it yields for the entropy:

$$s = -\frac{\partial \psi}{\partial T} = \frac{1}{\rho}\alpha \boldsymbol{I} : \boldsymbol{\sigma} + c_p \ln\left(\frac{T}{T_0}\right) + s_0, \tag{A.6}$$

or, in rate form:

$$\dot{s} = \frac{\partial s}{\partial \boldsymbol{\sigma}} : \dot{\boldsymbol{\sigma}} + \frac{\partial s}{\partial T}\dot{T} = \frac{1}{\rho}\alpha \boldsymbol{I} : \dot{\boldsymbol{\sigma}} + \frac{c_p}{T}\dot{T}. \tag{A.7}$$

Thus, inserting (A.7) into (A.4) eventually leads to the specific form of the heat equation for the proposed model, which is given in equation (14).

Appendix B. Numerical implementation: Backward Euler time implicit algorithm

Let's recall that a FE solver, like *ABAQUS/Standard*, employs a backward Euler (or time-implicit) integration scheme. Accordingly, the value of a given quantity x is computed from the previous time increment n to the current one $n+1$ such that $x^{(n+1)} = x^{(n)} + \Delta x^{(n+1)}$. Such a relationship is usually solved through an iterative scheme. Therefore, the current value of x is corrected for each iteration k by: $x^{(n+1)(k+1)} = x^{(n+1)(k)} + \delta x^{(n+1)(k)}$ or $\Delta x^{(n+1)(k+1)} = \Delta x^{(n+1)(k)} + \delta x^{(n+1)(k)}$ until $x^{(n+1)}$ converges.

When the analysis is completed at the time increment, n, the FE solver provides, for each integration point, all the state variables at the time increment n along with the increment of total strain $\Delta\boldsymbol{\varepsilon}^{(n+1)}$ and the increment of temperature $\Delta T^{(n+1)}$. From these data, the role of the UMAT subroutine is to compute: i) the stress and the state variables at the time increment $n+1$, and ii) the tangent operators $\mathbb{C}^{\boldsymbol{tg}}_{\boldsymbol{\sigma\varepsilon}} = \dfrac{\mathrm{d}\boldsymbol{\sigma}}{\mathrm{d}\boldsymbol{\varepsilon}}$ and $\boldsymbol{C}^{\boldsymbol{tg}}_{\boldsymbol{\sigma T}} = \dfrac{\mathrm{d}\boldsymbol{\sigma}}{\mathrm{d}T}$ that are necessary to achieve a fast convergence for the next FE calculation step.

B.1. Residuals

The equations governing the evolutions of the state variables are written under the form of residual functions that must satisfy a nullity condition. The one related to the recovery variable equation (11) gives:

$$\phi_\beta(T, \beta, \dot{\beta}, p) = \dot{\beta} - g(T) \times h(p - \beta). \tag{B.1}$$

For the plasticity, the residual function is simply equal to the yield function (8), which takes negative values when the material is not actively yielding, or that must remain null when actively yielding:

$$\phi_p(\boldsymbol{\sigma}, p, \beta) = f(\boldsymbol{\sigma}, p, \beta) = \mathrm{eq}(\boldsymbol{\sigma}) - R(p - \beta) - R_0. \tag{B.2}$$

B.2. Linearization of the constitutive equations

The implicit implementation of the proposed model requires to linearize the above residuals, as well as the stress. It is recalled that the *convex cutting plane* method (Simo and Ortiz, 1985; Ortiz and Simo, 1986; Simo and Hughes, 1998) considers a simplification regarding the linearization of the flow equation (9), in which the gradient of the plastic strain flow with respect to the stress is ignored. This gives:

$$\delta\boldsymbol{\varepsilon_p} = \boldsymbol{\Lambda}(\boldsymbol{\sigma})\delta p, \tag{B.3}$$

Therefore, one obtains the following linearized forms for the residuals and the stress:

$$\begin{aligned}\delta\phi_\beta &= \frac{\partial\phi_\beta}{\partial T}\delta T + \frac{\partial\phi_\beta}{\partial\beta}\delta\beta + \frac{\partial\phi_\beta}{\partial\dot{\beta}}\delta\dot{\beta} + \frac{\partial\phi_\beta}{\partial p}\delta p \\ &= \frac{\partial\phi_\beta}{\partial T}\delta T + \frac{\partial\phi_\beta}{\partial\beta}\delta\beta + \frac{\partial\phi_\beta}{\partial\dot{\beta}}\frac{1}{\Delta t}\delta\beta + \frac{\partial\phi_\beta}{\partial p}\delta p \\ &= \frac{\partial\phi_\beta}{\partial T}\delta T + \left(\frac{\partial\phi_\beta}{\partial\beta} + \frac{\partial\phi_\beta}{\partial\dot{\beta}}\frac{1}{\Delta t}\right)\delta\beta + \frac{\partial\phi_\beta}{\partial p}\delta p \\ &= A_{\beta T}\delta T + A_{\beta\beta}\delta\beta + A_{\beta p}\delta p,\end{aligned} \tag{B.4}$$

$$\begin{aligned}\delta\phi_p &= \frac{\partial\phi_p}{\partial\boldsymbol{\sigma}} : \delta\boldsymbol{\sigma} + \frac{\partial\phi_p}{\partial p}\delta p + \frac{\partial\phi_p}{\partial\beta}\delta\beta \\ &= \boldsymbol{A_{p\sigma}} : \delta\boldsymbol{\sigma} + A_{pp}\delta p + A_{p\beta}\delta\beta,\end{aligned} \tag{B.5}$$

$$\begin{aligned}\delta\boldsymbol{\sigma} &= \frac{\partial\boldsymbol{\sigma}}{\partial\boldsymbol{\varepsilon}} : \delta\boldsymbol{\varepsilon} + \frac{\partial\boldsymbol{\sigma}}{\partial T}\delta T + \frac{\partial\boldsymbol{\sigma}}{\partial\boldsymbol{\varepsilon_p}} : \delta\boldsymbol{\varepsilon_p} \\ &= \frac{\partial\boldsymbol{\sigma}}{\partial\boldsymbol{\varepsilon}} : \delta\boldsymbol{\varepsilon} + \frac{\partial\boldsymbol{\sigma}}{\partial T}\delta T + \frac{\partial\boldsymbol{\sigma}}{\partial\boldsymbol{\varepsilon_p}} : \boldsymbol{\Lambda}(\boldsymbol{\sigma})\delta p \\ &= \mathbb{B}_{\boldsymbol{\sigma\varepsilon}} : \delta\boldsymbol{\varepsilon} + \boldsymbol{B_{\sigma T}}\delta T + \boldsymbol{B_{\sigma p}}\delta p,\end{aligned} \tag{B.6}$$

where

$$A_{\beta T} = \frac{\partial\phi_\beta}{\partial T} = -\frac{\partial g}{\partial T} \times h(p-\beta), \tag{B.7a}$$

$$A_{\beta\beta} = \frac{\partial\phi_\beta}{\partial\beta} + \frac{\partial\phi_\beta}{\partial\dot{\beta}}\frac{1}{\Delta t} = -g(T) \times \frac{\partial h}{\partial\beta} + \frac{1}{\Delta t}, \tag{B.7b}$$

$$A_{\beta p} = \frac{\partial\phi_\beta}{\partial p} = -g(T) \times \frac{\partial h}{\partial p}, \tag{B.7c}$$

$$\boldsymbol{A_{p\sigma}} = \frac{\partial\phi_p}{\partial\boldsymbol{\sigma}} = \boldsymbol{\Lambda}(\boldsymbol{\sigma}), \tag{B.8a}$$

$$A_{pp} = \frac{\partial\phi_p}{\partial p} = \frac{\partial R}{\partial p}, \tag{B.8b}$$

$$A_{p\beta} = \frac{\partial \phi_p}{\partial \beta} = \frac{\partial R}{\partial \beta}, \tag{B.8c}$$

$$\mathbb{B}_{\boldsymbol{\sigma\varepsilon}} = \frac{\partial \boldsymbol{\sigma}}{\partial \boldsymbol{\varepsilon}} = \mathbb{C}, \tag{B.9a}$$

$$\boldsymbol{B_{\sigma T}} = \frac{\partial \boldsymbol{\sigma}}{\partial T} = -\mathbb{C} : \alpha \boldsymbol{I}, \tag{B.9b}$$

$$\boldsymbol{B_{\sigma p}} = \frac{\partial \boldsymbol{\sigma}}{\partial \boldsymbol{\varepsilon_p}} : \boldsymbol{\Lambda}(\boldsymbol{\sigma}) = -\mathbb{C} : \boldsymbol{\Lambda}(\boldsymbol{\sigma}). \tag{B.9c}$$

B.3. Computation of the stress

B.3.1. Elastic prediction with hardening recovery correction

During this first step, the material is assumed to behave elastically in order to assess if it is actively yielding or not. Thus, the plasticity-related internal state variables $\boldsymbol{\varepsilon_p}$ and p are kept constant, while the recovery variable β can evolve. Since the evolution of β does not influence the elastic behavior of the material, a first correction of β can be done prior to the elastic prediction. To initiate the correction procedure for β, its value is kept constant at first, which leads to a non-null residual ϕ_β. Therefore, β is iteratively updated (k loop) until ϕ_β is sufficiently close to 0. This gives:

$$\beta^{(n+1)(k+1)} = \beta^{(n+1)(k)} + \delta\beta^{(n+1)(k)}. \tag{B.10}$$

In this update procedure, $\delta\beta$ is obtained from the nullity condition of the residual ϕ_β (all the quantities are taken at $^{(n+1)(k)}$):

$$\phi_\beta + \delta\phi_\beta = 0, \tag{B.11}$$

where $\delta\phi_\beta$ is expressed from the linearization of ϕ_β, given in (B.4), while considering $\delta T = 0$ and $\delta p = 0$:

$$\delta\phi_\beta = A_{\beta\beta}\delta\beta. \tag{B.12}$$

Therefore, inserting (B.12) into (B.11) leads to the expression for $\delta\beta$:

$$\delta\beta = \frac{-\phi_\beta}{A_{\beta\beta}}, \tag{B.13}$$

where the term $A_{\beta\beta}$ is provided in (B.7b). Once converged, the stress can be elastically predicted with the equation (4). Then, the residual ϕ_p is calculated with the equation (B.2) in order to assess whether the material is actively yielding or not:

- if $\phi_p < 0$, then the plasticity is not active and the stress does not need to be corrected.
- if $\phi_p > 0$, then the plasticity is active and the stress needs to be corrected. This is the purpose of the second step refereed to as *plastic and hardening recovery correction*.

B.3.2. Plastic and hardening recovery correction

During this second step, the plasticity-related internal state variables $\boldsymbol{\varepsilon_p}$ and p, as well as the recovery variable β can simultaneously evolve. Therefore all the internal state variables are iteratively updated (k loop) until both ϕ_β and ϕ_p are sufficiently close to 0. This gives:

$$\beta^{(n+1)(k+1)} = \beta^{(n+1)(k)} + \delta\beta^{(n+1)(k)}, \tag{B.14a}$$

$$p^{(n+1)(k+1)} = p^{(n+1)(k)} + \delta p^{(n+1)(k)}, \tag{B.14b}$$

$$\boldsymbol{\varepsilon_p}^{(n+1)(k+1)} = \boldsymbol{\varepsilon_p}^{(n+1)(k)} + \delta\boldsymbol{\varepsilon_p}^{(n+1)(k)}. \tag{B.14c}$$

In this update procedure, $\delta\beta$, δp and $\delta\boldsymbol{\varepsilon_p}$ are obtained from the nullity conditions of both residuals ϕ_β and ϕ_p (all the quantities are taken at $^{(n+1)(k)}$):

$$\begin{cases} \phi_\beta + \delta\phi_\beta = 0 \\ \phi_p + \delta\phi_p = 0 \end{cases}, \tag{B.15}$$

where $\delta\phi_\beta$ and $\delta\phi_p$ are expressed from the linearizations of ϕ_β, ϕ_p and $\boldsymbol{\sigma}$, given in (B.4), (B.5) and (B.6), while considering $\delta\boldsymbol{\varepsilon} = \mathbf{0}$ and $\delta T = 0$:

$$\begin{cases} \delta\phi_\beta = A_{\beta\beta}\delta\beta + A_{\beta p}\delta p \\ \delta\phi_p = \boldsymbol{A_{p\sigma}} : \delta\boldsymbol{\sigma} + A_{pp}\delta p + A_{p\beta}\delta\beta \end{cases}, \tag{B.16}$$

and

$$\delta\boldsymbol{\sigma} = \boldsymbol{B_{\sigma p}}\delta p. \tag{B.17}$$

Therefore, inserting (B.16) and (B.17) into (B.15) leads to the following expression for $\delta\beta$ and δp:

$$\begin{Bmatrix} \delta\beta \\ \delta p \end{Bmatrix} = \begin{pmatrix} L_{\beta\beta} & L_{\beta p} \\ L_{p\beta} & L_{pp} \end{pmatrix} \times \begin{Bmatrix} -\phi_\beta \\ -\phi_p \end{Bmatrix}, \tag{B.18}$$

with

$$\begin{pmatrix} L_{\beta\beta} & L_{\beta p} \\ L_{p\beta} & L_{pp} \end{pmatrix} = \begin{pmatrix} K_{\beta\beta} & K_{\beta p} \\ K_{p\beta} & K_{pp} \end{pmatrix}^{-1}, \tag{B.19}$$

and

$$K_{\beta\beta} = A_{\beta\beta}, \quad K_{\beta p} = A_{\beta p}, \quad K_{p\beta} = A_{p\beta}, \quad K_{pp} = \boldsymbol{A_{p\sigma}} : \boldsymbol{B_{\sigma p}} + A_{pp}. \tag{B.20}$$

Furthermore, according to the *convex cutting plane* method (Simo and Ortiz, 1985; Ortiz and Simo, 1986; Simo and Hughes, 1998), $\delta\boldsymbol{\varepsilon_p}$ is directly connected to δp through the linearization of the flow equation (B.3)[3]

[3]Note that, according to the *convex cutting plane* method (Simo and Ortiz, 1985; Ortiz and Simo, 1986; Simo and Hughes, 1998) , the linearization of the flow equation (B.3) is explicitly integrated within the correction procedure. Nevertheless, the time integration is still implicit. Despite this simplification, the *convex cutting plane* method keeps a good accuracy when compared to other schemes, while involving less computational cost (Qidwai and Lagoudas, 2000).

B.4. Tangent operators

As previously mentioned, the proposed implementation is based on the *convex cutting plane* form of the *return mapping algorithm* (Simo and Ortiz, 1985; Ortiz and Simo, 1986; Simo and Hughes, 1998), which utilizes continuous tangent operators. Accordingly, in the present case, the formulations of the tangent operators $\mathbb{C}^{\boldsymbol{tg}}_{\boldsymbol{\sigma\varepsilon}} = \dfrac{\mathrm{d}\boldsymbol{\sigma}}{\mathrm{d}\boldsymbol{\varepsilon}}$ and $\boldsymbol{C}^{\boldsymbol{tg}}_{\boldsymbol{\sigma T}} = \dfrac{\mathrm{d}\boldsymbol{\sigma}}{\mathrm{d}T}$ are obtained by identifying a linear relationship between $\mathrm{d}\boldsymbol{\sigma}$, $\mathrm{d}\boldsymbol{\varepsilon}$ and $\mathrm{d}T$ such as:

$$\mathrm{d}\boldsymbol{\sigma} = \mathbb{C}^{\boldsymbol{tg}}_{\boldsymbol{\sigma\varepsilon}} : \mathrm{d}\boldsymbol{\varepsilon} + \boldsymbol{C}^{\boldsymbol{tg}}_{\boldsymbol{\sigma T}}\mathrm{d}T. \tag{B.21}$$

To do so, the stress strain temperature relationship is written in differential form. From equation (B.6), this gives:

$$\mathrm{d}\boldsymbol{\sigma} = \mathbb{B}_{\boldsymbol{\sigma\varepsilon}} : \mathrm{d}\boldsymbol{\varepsilon} + \boldsymbol{B}_{\boldsymbol{\sigma T}}\mathrm{d}T + \boldsymbol{B}_{\boldsymbol{\sigma p}}\mathrm{d}p. \tag{B.22}$$

If the plasticity is not active (the computation of the stress stopped at the *elastic prediction with hardening recovery correction*), then $\mathrm{d}p = 0$ and the tangent operators can be directly identified from equation (B.22) by $\mathbb{C}^{\boldsymbol{tg}}_{\boldsymbol{\sigma\varepsilon}} = \mathbb{B}_{\boldsymbol{\sigma\varepsilon}}$ and $\boldsymbol{C}^{\boldsymbol{tg}}_{\boldsymbol{\sigma T}} = \boldsymbol{B}_{\boldsymbol{\sigma T}}$. However, if the plasticity is active, (the computation of the stress went through the *plastic and hardening recovery correction*), then it becomes necessary to consider the simultaneous nullity conditions of the residuals ϕ_β and ϕ_p in their differential form. From equations (B.4) and (B.5), this gives:

$$\begin{cases} \mathrm{d}\phi_\beta = A_{\beta T}\mathrm{d}T + A_{\beta\beta}\mathrm{d}\beta + A_{\beta p}\mathrm{d}p = 0 \\ \mathrm{d}\phi_p = \boldsymbol{A}_{\boldsymbol{p\sigma}} : \mathrm{d}\boldsymbol{\sigma} + A_{pp}\mathrm{d}p + A_{p\beta}\mathrm{d}\beta = 0 \end{cases}. \tag{B.23}$$

Inserting (B.22) into (B.23), it yields:

$$\begin{Bmatrix} \mathrm{d}\beta \\ \mathrm{d}p \end{Bmatrix} = \begin{pmatrix} \boldsymbol{X}_{\boldsymbol{\beta\varepsilon}} & X_{\beta T} \\ \boldsymbol{X}_{\boldsymbol{p\varepsilon}} & X_{pT} \end{pmatrix} \times \begin{Bmatrix} \mathrm{d}\boldsymbol{\varepsilon} \\ \mathrm{d}T \end{Bmatrix}, \tag{B.24}$$

with

$$\begin{pmatrix} \boldsymbol{X}_{\boldsymbol{\beta\varepsilon}} & X_{\beta T} \\ \boldsymbol{X}_{\boldsymbol{p\varepsilon}} & X_{pT} \end{pmatrix} = - \begin{pmatrix} L_{\beta\beta} & L_{\beta p} \\ L_{p\beta} & L_{pp} \end{pmatrix} \times \begin{pmatrix} \boldsymbol{K}_{\boldsymbol{\beta\varepsilon}} & K_{\beta T} \\ \boldsymbol{K}_{\boldsymbol{p\varepsilon}} & K_{pT} \end{pmatrix}, \tag{B.25}$$

where the terms $L_{\beta\beta}$, $L_{\beta p}$, $L_{p\beta}$ and L_{pp} are given in (B.19), and:

$$\boldsymbol{K}_{\boldsymbol{\beta\varepsilon}} = \boldsymbol{0}, \quad K_{\beta T} = A_{\beta T}, \quad \boldsymbol{K}_{\boldsymbol{p\varepsilon}} = \boldsymbol{A}_{\boldsymbol{p\sigma}} : \mathbb{B}_{\boldsymbol{\sigma\varepsilon}}, \quad K_{pT} = \boldsymbol{A}_{\boldsymbol{p\sigma}} : \boldsymbol{B}_{\boldsymbol{\sigma T}}. \tag{B.26}$$

Finally, substituting dp in (B.22) with (B.24) allows to identify the following expressions for the tangent operators:

$$\mathbb{C}^{\boldsymbol{tg}}_{\boldsymbol{\sigma\varepsilon}} = \mathbb{B}_{\boldsymbol{\sigma\varepsilon}} + \boldsymbol{B}_{\boldsymbol{\sigma p}} \otimes \boldsymbol{X}_{\boldsymbol{p\varepsilon}} \qquad \text{and} \qquad \boldsymbol{C}^{\boldsymbol{tg}}_{\boldsymbol{\sigma T}} = \boldsymbol{B}_{\boldsymbol{\sigma T}} + \boldsymbol{B}_{\boldsymbol{\sigma p}} X_{pT}. \tag{B.27}$$

References

Aifantis, E.C., 1987. The physics of plastic deformation. International Journal of Plasticity 3, 211–247.

Bergheau, J.M., Vincent, Y., Leblond, J.B., Jullien, J.F., 2004. Viscoplastic behaviour of steels during welding. Science and Technology of Welding and Joining 9, 323–330.

Besson, J., Cailletaud, G., Chaboche, J.L., Forest, S., Blétry, M., 2010. Non-linear mechanics of materials. Solid mechanics and its applications, Springer, Dordrecht.

Blaizot, J., Chaise, T., Nélias, D., Perez, M., Cazottes, S., Chaudet, P., 2016. Constitutive model for nickel alloy 690 (Inconel 690) at various strain rates and temperatures. International Journal of Plasticity 80, 139–153.

Bru, D., Devaux, J., Bergheau, J.M., Pont, D., 1996. Influence of material properties at high temperatures on the modelling of welding residual stress and deformation state, in: Mathematical Modelling of Weld Phenomena. Institute of Materials. volume 3, pp. 456–463.

Chaboche, J., 2008. A review of some plasticity and viscoplasticity constitutive theories. International Journal of Plasticity 24, 1642–1693.

Chaboche, J.L., Nouailhas, D., 1989. A Unified Constitutive Model for Cyclic Viscoplasticity and Its Applications to Various Stainless Steels. Journal of Engineering Materials and Technology 111, 424.

Chatzigeorgiou, G., Charalambakis, N., Chemisky, Y., Meraghni, F., 2018. Thermomechanical Behavior of Dissipative Composite Materials. Elsevier.

Chen, X.M., Lin, Y., Wen, D.X., Zhang, J.L., He, M., 2014. Dynamic recrystallization behavior of a typical nickel-based superalloy during hot deformation. Materials & Design 57, 568–577.

Chetra Mang, Hindili, S., 2017. Modèle de comportement élastoplastique adapté à la simulation numérique du soudage, Giens, Var, France.

Depradeux, L., 2004. Simulation numérique du soudage - acier 316L - Validation sur cas tests de complexité croissante. Ph.D. thesis. Ecole doctorale des sciences de l'ingénieur de Lyon. Lyon.

Depradeux, L., Coquard, R., 2018. Influence of viscoplasticity, hardening, and annealing effects during the welding of a three-pass slot weld (NET-TG4 round robin). International Journal of Pressure Vessels and Piping 164, 39–54.

Eagar, T., Tsai, N., 1983. Temperature Fields Produced by Traveling Distributed Heat Sources. Welding Journal. Welding Journal 62, 346–355.

Estrin, Y., Mecking, H., 1984. A unified phenomenological description of work hardening and creep based on one-parameter models. Acta Metallurgica 32, 57–70.

Farzadi, A., 2015. Modeling of isothermal recovery and recrystallization kinetics by means of hardness measurements: Modell zur isothermen Erholung und Rekristallisationskinetiken anhand von Härtemessungen. Materialwissenschaft und Werkstofftechnik 46, 1218–1225.

Friedel, J., 1964. Dislocations. Pergamon, Oxford.

Goldak, J., Chakravarti, A., Bibby, M., 1984. A new finite element model for welding heat sources. Metallurgical Transactions B 15, 299–305.

Goldak, J.A., Akhlaghi, M., 2005. Computational Welding Mechanics. Springer Science, Business Media, Inc., Boston, MA.

Humphreys, F.J., 2017. Recrystallization and Related Annealing Phenomena. Third ed., Elsevier, Amsterdam, Netherlands.

Joosten, M.M., Gallegillo, M.S., 2012. A Study of the Effect of Hardening Model in the Prediction of Welding Residual Stress, in: Volume 6: Materials and Fabrication, Parts A and B, ASME, Toronto, Ontario, Canada.

Keavey, M., Mark, A., Dai, H., Withers, P.J., 2010. Annealing Models in Welding Simulation: Conservative and Non-Conservative Residual Stress Distributions, in: ASME 2010 Pressure Vessels and Piping Conference:

Volume 6, Parts A and B, ASME, Bellevue, Washington, USA. pp. 1377–1384.

Kocks, U., Mecking, H., 2003. Physics and phenomenology of strain hardening: the FCC case. Progress in Materials Science 48, 171–273.

Leblond, J.B., Pont, D., Bergheau, J.M., 1997. Metallurgical and mechanical consequences of phase transformations in numerical simulations of welding processes, in: Modeling in Welding, Hot Powder Forming and Casting, pp. 61–89.

Leggatt, R., 2008. Residual stresses in welded structures. International Journal of Pressure Vessels and Piping 85, 144–151.

Lemaître, J., Chaboche, J.L., 1990. Mechanics of solid materials. Cambridge University Press, Cambridge.

Levenberg, K., 1944. A method for the solution of certain non-linear problems in least squares. Quarterly of Applied Mathematics 2, 164–168.

Lin, Y., Dong, W.Y., Zhou, M., Wen, D.X., Chen, D.D., 2018. A unified constitutive model based on dislocation density for an Al-Zn-Mg-Cu alloy at time-variant hot deformation conditions. Materials Science and Engineering: A 718, 165–172.

Lindgren, L.E., 2007. Computational welding mechanics: thermomechanical and microstructural simulations. Woodhead Publ., Cambridge.

Lindgren, L.E., Domkin, K., Hansson, S., 2008. Dislocations, vacancies and

solute diffusion in physical based plasticity model for AISI 316l. Mechanics of Materials 40, 907–919.

Lindgren, L.E., Hao, Q., Wedberg, D., 2017. Improved and simplified dislocation density based plasticity model for AISI 316 L. Mechanics of Materials 108, 68–76.

Lindgren, L.E., Runnemalm, H., Näsström, M.O., 1999. Simulation of multipass welding of a thick plate. International Journal for Numerical Methods in Engineering 44, 1301–1316.

Marquardt, D.W., 1963. An Algorithm for Least-Squares Estimation of Nonlinear Parameters. Journal of the Society for Industrial and Applied Mathematics 11, 431–441.

Mecking, H., Kocks, U., 1981. Kinetics of flow and strain-hardening. Acta Metallurgica 29, 1865–1875.

Meraghni, F., Chemisky, Y., Piotrowski, B., Echchorfi, R., Bourgeois, N., Patoor, E., 2014. Parameter identification of a thermodynamic model for superelastic shape memory alloys using analytical calculation of the sensitivity matrix. European Journal of Mechanics - A/Solids 45, 226–237.

Messerschmidt, U., Hull, R., Jagadish, C., Osgood, R., Parisi, J., Wang, Z., Warlimont, H., 2010. Dislocation Dynamics During Plastic Deformation. volume 129. Springer, Berlin, Heidelberg.

Mochizuki, M., Matsushima, S., Toyoda, M., Zhang, Z., Gundersen, O., Thaulow, C., 2002. Generation Behavior of Thermal and Residual Stresses

Due to Phase Transformation During Welding Heat Cycles, ASME, Vancouver, BC, Canada. pp. 123–129.

Mullins, J., Gunnars, J., 2009. Influence of Hardening Model on Weld Residual Stress Distribution. Technical Report 2009:16. Inspecta Technology AB. Stockholm, Sweden.

Murugan, S., Kumar, P., Raj, B., Bose, M., 1998. Temperature distribution during multipass welding of plates. International Journal of Pressure Vessels and Piping 75, 891–905.

Muránsky, O., Hamelin, C., Patel, V., Luzin, V., Braham, C., 2015. The influence of constitutive material models on accumulated plastic strain in finite element weld analyses. International Journal of Solids and Structures 69-70, 518–530.

Muránsky, O., Hamelin, C., Smith, M., Bendeich, P., Edwards, L., 2012a. The effect of plasticity theory on predicted residual stress fields in numerical weld analyses. Computational Materials Science 54, 125–134.

Muránsky, O., Smith, M., Bendeich, P., Holden, T., Luzin, V., Martins, R., Edwards, L., 2012b. Comprehensive numerical analysis of a three-pass bead-in-slot weld and its critical validation using neutron and synchrotron diffraction residual stress measurements. International Journal of Solids and Structures 49, 1045–1062.

Nes, E., 1997. Modelling of work hardening and stress saturation in FCC metals. Progress in Materials Science 41, 129–193.

Orowan, E., 1940. Problems of plastic gliding. Proceedings of the Physical Society 52, 8–22.

Ortiz, M., Simo, J.C., 1986. An analysis of a new class of integration algorithms for elastoplastic constitutive relations. International Journal for Numerical Methods in Engineering 23, 353–366.

Petkovic, R., Luton, M., Jonas, J., 1979. Recovery and recrystallization of polycrystalline copper after hot working. Acta Metallurgica 27, 1633–1648.

Pham, M.S., Iadicola, M., Creuziger, A., Hu, L., Rollett, A.D., 2015. Thermally-activated constitutive model including dislocation interactions, aging and recovery for strain path dependence of solid solution strengthened alloys: Application to AA5754-O. International Journal of Plasticity 75, 226–243.

Praud, F., 2018. Multi-scale modelling of thermoplastic-based woven composites, cyclic and time-dependent behaviour. Ph.D. thesis. Arts et Métiers ParisTech.

Praud, F., Chatzigeorgiou, G., Bikard, J., Meraghni, F., 2017a. Phenomenological multi-mechanisms constitutive modelling for thermoplastic polymers, implicit implementation and experimental validation. Mechanics of Materials 114, 9–29.

Praud, F., Chatzigeorgiou, G., Chemisky, Y., Meraghni, F., 2017b. Hybrid micromechanical-phenomenological modelling of anisotropic damage and anelasticity induced by micro-cracks in unidirectional composites. Composite Structures 182, 223–236.

Qidwai, M.A., Lagoudas, D.C., 2000. Numerical implementation of a shape memory alloy thermomechanical constitutive model using return mapping algorithms. International Journal for Numerical Methods in Engineering 47, 1123–1168.

Razakanaivo, A., Waeckel, F., 1999. A viscoplastic model for numerical simulation of welding and post-weld heat treatment. Le Journal de Physique IV 09, Pr9–371–Pr9–381.

Satoh, K., Ohnishi, T., 1972. Transient thermal stresses of Weld Heat-Affected Zone by Both-Ends Fixed Bar Analogy. Transactions of Japan Welding Society 3, 125–134.

Seleš, K., Perić, M., Tonković, Z., 2018. Numerical simulation of a welding process using a prescribed temperature approach. Journal of Constructional Steel Research 145, 49–57.

Simo, J., Ortiz, M., 1985. A unified approach to finite deformation elastoplastic analysis based on the use of hyperelastic constitutive equations. Computer Methods in Applied Mechanics and Engineering 49, 221–245.

Simo, J.C., Hughes, T.J.R., 1998. Computational inelasticity. Springer, New York.

Smith, M., Bouchard, P., Turski, M., Edwards, L., Dennis, R., 2012. Accurate prediction of residual stress in stainless steel welds. Computational Materials Science 54, 312–328.

Smith, M.C., Nadri, B., Smith, A.C., Carr, D.G., Bendeich, P.J., Edwards,

L.E., 2009. Optimisation of Mixed Hardening Material Constitutive Models for Weld Residual Stress Simulation Using the NeT Task Group 1 Single Bead on Plate Benchmark Problem, ASME. pp. 303–318.

Stüwe, H., Padilha, A., Siciliano, F., 2002. Competition between recovery and recrystallization. Materials Science and Engineering: A 333, 361–367.

Suwas, S., Ray, R.K., 2014. Crystallographic texture of materials. Springer, London.

Vandermeer, R.A., Rath, B.B., 1990. Interface migration during recrystallization: The role of recovery and stored energy gradients. Metallurgical Transactions A 21, 1143–1149.

Voyiadjis, G., Abed, F., 2005. Effect of dislocation density evolution on the thermomechanical response of metals with different crystal structures at low and high strain rates and temperatures. Archives of Mechanics 57, 299–343.

Voyiadjis, G.Z., Song, Y., Rusinek, A., 2019. Constitutive model for metals with dynamic strain aging. Mechanics of Materials 129, 352–360.

Yu, X., Crooker, P., Wang, Y., Feng, Z., 2015. High-Temperature Deformation Constitutive Law for Dissimilar Weld Residual Stress Modeling: Effect of Thermal Load on Strain Hardening, in: Volume 6B: Materials and Fabrication, ASME, Boston, Massachusetts, USA.

Yuan, K., Guo, W., Li, P., Zhang, Y., Li, X., Lin, X., 2019. Thermomechanical behavior of laser metal deposited Inconel 718 superalloy over a wide

range of temperature and strain rate: Testing and constitutive modeling. Mechanics of Materials 135, 13–25.

Conflict of Interest and Authorship Conformation Form

Please check the following as appropriate:

- o All authors have participated in (a) conception and design, or analysis and interpretation of the data; (b) drafting the article or revising it critically for important intellectual content; and (c) approval of the final version.
- o This manuscript has not been submitted to, nor is under review at, another journal or other publishing venue.
- o The authors have no affiliation with any organization with a direct or indirect financial interest in the subject matter discussed in the manuscript
- o The following authors have affiliations with organizations with direct or indirect financial interest in the subject matter discussed in the manuscript:

Author's name	Affiliation
Loic Mouelle	LEM3 - UL
Francis Praud	ENSAM
Georges Chatzigeorgiou	LEM3 - ENSAM
Fodil Meraghni	LEM3 - ENSAM
Jérome Serri	LEM3 - UL
Eric Fleury	LEM3 - UL